Published in final edited form as:
Phys Med Biol. 2013 June 7; 58(11): 3791–3814. doi:10.1088/0031-9155/58/11/3791.

NEMA NU-4 performance evaluation of PETbox4, a high sensitivity dedicated PET preclinical tomograph

Z Gu[1], **R Taschereau**[1], **N T Vu**[2], **H Wang**[1], **D L Prout**[1], **R W Silverman**[1], **B Bai**[3], **D B Stout**[1,2], **M E Phelps**[1,2], and **A F Chatziioannou**[1,2]

Z Gu: zhgu@mednet.ucla.edu

[1]Crump Institute for Molecular Imaging, David Geffen School of Medicine, University of California at Los Angeles, Los Angeles, CA, USA

[2]Sofie Biosciences, Culver City, California, USA

[3]Keck School of Medicine, University of Southern California, Los Angeles, CA, USA

Abstract

PETbox4 is a new, fully tomographic bench top PET scanner dedicated to high sensitivity and high resolution imaging of mice. This manuscript characterizes the performance of the prototype system using the National Electrical Manufacturers Association (NEMA) NU 4–2008 standards, including studies of sensitivity, spatial resolution, energy resolution, scatter fraction, count-rate performance and image quality. The PETbox4 performance is also compared with the performance of PETbox, a previous generation limited angle tomography system. PETbox4 consists of four opposing flat-panel type detectors arranged in a box like geometry. Each panel is made by a 24 × 50 pixelated array of 1.82 × 1.82 × 7mm bismuth germanate (BGO) scintillation crystals with a crystal pitch of 1.90mm. Each of these scintillation arrays is coupled to two Hamamatsu H8500 photomultiplier tubes via a glass light guide. Volumetric images for a 45 × 45 × 95 mm field of view (FOV) are reconstructed with a maximum likelihood expectation maximization (ML-EM) algorithm incorporating a system model based on a parameterized detector response. With an energy window of 150–650 keV, the peak absolute sensitivity is approximately 18% at the center of FOV. The measured crystal energy resolution ranges from 13.5% to 48.3% full width at half maximum (FWHM), with a mean of 18.0%. The intrinsic detector spatial resolution is 1.5mm FWHM in both transverse and axial directions. The reconstructed image spatial resolution for different locations in the FOV ranges from 1.32mm to 1.93 mm, with an average of 1.46 mm. The peak noise equivalent count rate for the mouse-sized phantom is 35 kcps for a total activity of 1.5 MBq (40 μCi) and the scatter fraction is 28%. The standard deviation in the uniform region of the image quality phantom is 5.7%. The recovery coefficients range from 0.10 to 0.93. In comparison to the first generation two panel PETbox system, PETbox4 achieves substantial improvements on sensitivity and spatial resolution. The

(A video clip can be accessed online as the supplementary data enhancement)

Conflict of Interest Disclosure.
The PETbox4 technology presented in this manuscript has been commercialized by Sofie Biosciences, Inc., Culver City, CA, USA. Nam T. Vu is currently an employee of Sofie Biosciences, Inc., and Nam T. Vu, Michael E. Phelps, David B. Stout and Arion F. Chatziioannou are shareholders of Sofie Biosciences, Inc.

overall performance demonstrates that the PETbox4 scanner is suitable for producing high quality images for molecular imaging based biomedical research.

1. Introduction

Positron emission tomography (PET) is an imaging modality that enables non-invasive, in vivo detection and quantification of biological processes at the molecular level and has found wide applications in pharmacology, genetics, and pathology investigations (Phelps, 2000; Gambhir, 2002; Myers, 2001; Chatziioannou, 2002a). Since the 1990s, significant efforts in the development of small animal PET prototype scanners have pushed the limits of resolution and sensitivity with various approaches (Bloomfield et al., 1995; Lecomte et al., 1996; Cherry et al., 1997; Chatziioannou et al., 1999; Jeavons et al., 1999; Weber et al., 2000; Di Domenico et al., 2003; Seidel et al., 2003; Surti et al., 2003; Tai et al., 2003; Correia et al., 2004; Rouze et al., 2004; Miyaoka et al., 2005; Schafers et al., 2005; Ziemons et al., 2005; Li et al., 2007; Bergeron et al., 2009; Lage et al., 2009; Prasad et al., 2010; Zhang et al., 2011; Szanda et al., 2011; Canadas et al., 2011; Sanchez et al., 2012). Commercial preclinical PET systems also became available since 2000 (Tai et al., 2001; Knoess et al., 2003; Tai et al., 2005; Laforest et al., 2007; Schafers et al., 2005; Wang et al., 2006; Huisman et al., 2007; de Jong et al., 2007; Bao et al., 2009; Canadas et al., 2011; Prasad et al., 2010, 2011; Szanda et al., 2011). The performance and capabilities of these systems evolved rapidly and have led to an increased use and acceptance of in vivo molecular imaging techniques in biological laboratories.

Advancements in molecular biology have made genetically modified mice the animal of choice to mimic human subjects for both healthy and diseased states (Paigen, 1995). The mouse genome was the second mammalian genome to be fully sequenced after the human (Marshall, 2001). The use of mouse models also has a relatively low cost of maintaining colonies due to the rapid reproduction and short normal life span of mice (Weissleder and Mahmood, 2001). It is worthwhile to note that genetically modified mice represent more than 90% of the preclinical disease models in biological research (Malakoff, 2000). The requirement to image in addition to mice, larger rodents such as rats, necessitates an enlarged imaging Field Of View (FOV), which leads to significantly larger detector surfaces, with tens of thousands of crystal elements and complicated electronics for most configurations, significantly increasing cost. Furthermore, the increased geometric detector separation leads to significant reduction to the system sensitivity, compromising performance. In this work, the design of the PETbox4 was optimized specifically for imaging mice, with a useful FOV that can accommodate the vast majority of mice (18–40g), therefore presents a compromise in the target subject size, in exchange for low cost and high sensitivity.

The volume and mass of mice are approximately 3000 times smaller than that of humans and 10– 20 times smaller than an average rat. The spatial resolution of a PET scanner dedicated for mouse imaging should be similarly higher and the voxel size in the reconstructed images should also be reduced according to sampling theory (Chatziioannou, 2002b). To obtain images of the same statistical quality as in humans, the number of counts

detected per voxel, which is inversely proportional to voxel volume, could be compensated by either increasing the radioactivity of injected probes or by improving the sensitivity of the scanner. However, with a typical amount of radioactivity administered (7.4 MBq (200 μCi)) (Chatziioannou et al 1999), the concentration of radionuclides in mice is already much higher than that in humans. It has been shown that during preclinical PET imaging procedures, major organs like the bladder, brain, heart, and tumor xenografts of mice could receive an absorbed dose in a range for which biological effects such as stimulated cell proliferation (Wang and Cai, 2000), induced radio-resistance (Yonezawa, 2006), elevated gene expression (Amundson et al., 2001), have been reported (Taschereau and Chatziioannou, 2007; Funk et al., 2004). Those biological effects may interfere and bias the results in pharmaceutical and genetic studies, leading to discrepancies on translational research between mouse models and clinical applications. Also, for many applications such as neuroreceptor imaging, the signal of concern can be inherently limited by the number of binding sites available, as well as by the specificity and affinity of the radiotracers (Hume et al., 1998). The injected probe mass, which should be below levels that perturb the studied biological system, may limit the amount of radioactivity that can be injected into a mouse to the range of 0.37–3.7MBq (10–100 μCi) (Hume et al., 1998). High sensitivity imaging systems are therefore desirable to obtain count statistics adequate per volumetric resolution element with lower amounts of radioactivity and reduce radiation dose delivered to mice. This is especially important in the case of longitudinal studies, in which multiple experiments take place over a period of time. In addition, high sensitivity also contributes to higher imaging throughput, by maintaining optimized imaging performance within the required scan time, which is especially important when imaging a considerable number of subjects in one study (Gagnon et al., 2009).

Combining these considerations, PETbox4, a bench top PET scanner dedicated to high sensitivity and high resolution imaging of mice, was recently designed and built at our institute. PETbox4 is configured using a close geometry of flat panel detectors to provide large solid angle coverage. The addition of a multiplexing scheme for each detector head allows for a low number of required electronic channels to be readout. These parameters provide a system with high performance, low cost and reduced complexity. For typical biodistribution studies in this system, we anticipate an administered radioactivity amount of less than 1.5 MBq (40 μCi), which is five times lower than established procedures. PETbox4 is the second generation of the previous prototype PETbox system developed by our group (Zhang et al., 2011; Zhang et al., 2010) and presents a significant improvement on sensitivity and spatial resolution. This work aims to characterize the overall performance of the PETbox4 system using the National Electrical Manufacturers Association (NEMA) NU 4–2008 standards wherever possible. The NEMA NU-4 standards offer a consistent and standardized methodology for small animal PET performance assessment, including sensitivity, spatial resolution, scatter fraction, count rate performance and image quality characteristics. Additional measurements were also performed: energy resolution and intrinsic detector spatial resolution. The overall imaging capabilities of the scanner and its suitability for high-sensitivity high-resolution molecular imaging were also demonstrated through in-vivo rodent studies.

2. Materials and methods

2.1. System description

PETbox4 employs four opposing panel detectors placed at a spacing of 5 cm, arranged in a compact, box like geometry (figure 1.(a)). The effective area of each scintillator array is 45.58 × 95.05 mm, large enough to cover the whole body of the vast majority of laboratory mice (18–40g). For the scintillator material of the detectors, bismuth germanate (BGO) was chosen. This scintillator has a high effective atomic number (Z=83) which increases the probability of a photoelectric event at the first interaction site and reduces inter-crystal scatter, leading to more accurate event positioning and higher spatial resolution. BGO also has an overall stopping power for 511 keV photons comparable to that of lutetium oxyorthosilicate (LSO). In previous work, we have shown that a BGO based scanner has higher system sensitivity and lower scatter fraction than the equivalent LSO based scanner (Bao and Chatziioannou 2007). To achieve equivalent sensitivity, a BGO system requires lower detector thickness, leading to reduced parallax errors and better spatial resolution. Additionally, BGO has about 35 times lower intrinsic radioactivity compared with LSO (de Marcillac et al., 2003). Therefore, the system background will not adversely affect the system minimum detectable activity (MDA) (Goertzen et al., 2007; Bao and Chatziioannou, 2010), especially when considering a very compact geometry and the intended use of the system at low activity levels. Each panel detector of the PETbox4 is comprised of a 24 × 50 pixelated BGO scintillator array with individual crystals measuring 1.82 × 1.82 × 7 mm (± 0.05mm) and a pitch of 1.90 mm (Proteus, Chagrin Falls, OH). The individual pixels are cut but not optically polished, and are separated by VM2000 a specular optical reflector (3M, St Paul, MN), generating optical properties that are a mixture of specular and diffuse reflection. The entire array is permanently coupled with a polymer silicon material to two H8500 multi-channel position-sensitive photomultiplier tubes (PSPMT; Hamamatsu Photonics, Bridgewater, NJ) via a glass light guide (figure 1.(b)). The read-out electronics of each detector are integrated in a compact printed circuit board stack directly attached to the PMT sockets. A charge-division readout circuit is used to convert the anode outputs from the two PSPMTs into position encoding signals, while the timing signal is obtained directly from the 12^{th} dynode signal on the H8500 PSPMTs. The four detector modules and the associated readout circuitry are encased in an aluminum housing and mounted on a frame.

Position and timing signals from the readout circuitry of the four panel detectors are digitized by sixteen 104-Mhz free running analog-to-digital converters (ADC) on an FPGA-based signal processing card (VHS-ADC, Lyrtech Signal Processing, Quebec City, Quebec). The digital samples are then processed in a Xilinx Virtex-4 field programmable gate array (Xilinx, San Jose, CA) in real time, including pulse shaping, event triggering, event qualification and coincidence detection. The 128 MB synchronous dynamic random access memory (SDRAM) on the VHS-ADC board stores look-up tables (LUT) that are applied to the digitized energy and position data for online identification of the crystal of interaction and for energy discrimination. A delayed window method is also implemented in the FPGA to estimate random coincidence event rates. A compactPCI CPU card (cPCI-6965, ADLINK, San Jose, CA) is used to control the FPGA logic on the VHS-ADC card, to

receive the generated 32-Bit list-mode data stream and to save the data to an external hard disk.

For the work described here, all measurements were acquired with a coincidence timing window of 20 nsec, and the acquired list-mode data were histogrammed into sinograms with delayed events subtracted to correct for random coincidences. Unless explicitly stated otherwise, all list-mode data measurements were acquired with an energy window of 150–650 keV, which is the default operating window for imaging with the PETbox4. The notable exception to this was the sensitivity measurement, for which the lower energy was varied, to show the influence of energy window on system sensitivity.

Component-based normalization (Mumcuoglu et al., 1994) was applied to compensate for the differences in individual detector efficiencies, estimated from measurements of a cylindrical source filled with ^{18}F. Fully 3D tomographic images were reconstructed by a maximum likelihood and expectation maximization (ML-EM) algorithm with the incorporation of a system model based on a parameterized detector response (Taschereau et al., 2011). For all studies in this paper, 60 iterations were used for the reconstruction of image data with no regularization. The resulting image matrix consisted of 96 × 96 × 200 voxel bins with a cubic voxel of 0.476 × 0.476 × 0.476 mm^3, forming an entire reconstructed FOV of 45 × 45 × 95 mm^3. Table 1 summarizes the geometric and physical characteristics of the PETbox4 and the first generation PETbox system.

The PETbox4 is integrated with a Mouse Atlas Registration System (MARS) which provides a novel anatomical reference approach via a combination of x-ray projection, optical photographic images and a digital mouse atlas (Wang et al., 2011; Wang et al., 2012). The MARS consists of a miniature x-ray tube (MAGNUM® 40 kV x-ray source, Moxtek Inc., UT, USA), an x-ray detector (RedEye™200 Remote Senor, Rad-icon Imaging Corp. CA, USA) and a webcam (Firefly® MV, Point Grey Research Inc., BC, Canada). The complete PETbox4/MARS system retains a small overall footprint, as shown in figure 2.

2.2. Energy resolution and Flood Histograms

A 0.106 MBq ^{68}Ge (2.86 μCi) cylinder source (Eckert & Ziegler Isotope Products, Valencia, CA) with a diameter of 32 mm and 67 mm length was placed at the center of the field of view (CFOV) of the system to acquire a two-dimensional flood image for each detector, for singles events. Boundaries were determined using a semi-automated program to define the crystal look-up tables (LUT) that classify regions in the flood image into the proper crystal of the BGO array. For this acquisition, specialized software was utilized on the system electronics, recording the energy of each event into the list mode data. Energy spectra of individual crystals were extracted based on the LUTs and a Gaussian function was fitted to the photopeak of each energy spectra. Energy resolution was measured for every crystal in the scanner as the full width at half-maximum (FWHM) of the Gaussian function divided by the energy corresponding to the center of the photopeak, expressed as a percentage resolution.

2.3. Spatial resolution

A 1.05 MBq (28.3 μCi) ^{22}Na point source with a nominal size of 0.3 mm, embedded in a 1cm^3 piece of acrylic was used (NEMA NU4 compliant, Eckert & Ziegler Isotope Products, Valencia, CA). The system was configured to acquire data in coincidence mode. Measurements were not corrected for the point source dimensions, positron range, or the non-collinearity of positron annihilation.

2.3.1. Intrinsic spatial resolution—Starting from the center of the FOV, the point source was attached to a translation stage and stepped at 0.4 mm steps across the mid line of two opposing panel detectors along the long axis of the system. An assumption was made that the detector coincidence pair configuration is symmetric and therefore measurements were performed for only half of the detector axial FOV. Due to geometric restriction by the two side detectors, the point source could not be stepped across half of the detector along the short axis. Instead, the source was stepped across the central fourteen crystals in the central axial plane. The acquisition time was 30 seconds at each location. The coincidence counts for directly opposing crystal pairs were plotted as a function of source location. The count distribution of each crystal pair was fitted with a Gaussian function and the FWHM was calculated to determine the intrinsic spatial resolution of the detectors.

2.3.2. Image spatial resolution—The point source was imaged at two axial locations: (a) the center of the axial FOV and (b) one fourth of the axial FOV, 23.5 mm from the center along the axial direction. For each of these two axial locations, the source was stepped in 5 mm increments toward the edge of the transverse FOV at the following radial distances from the geometric center: 0 mm, 5 mm, 10 mm, 15 mm and 20 mm. Acquisition time was 1 minute at each position and more than 10^5 prompt counts were acquired per measurement. The NEMA NU-4 document also recommends a measurement at 25 mm from the center, which was out of the transaxial FOV of the PETbox4 and is therefore not included in this study.

The list-mode data acquired at each position were histogrammed into sinograms with delayed events subtracted to correct for random coincidences and with a normalization to compensate for the differences in individual detector efficiencies. The images were reconstructed using the ML–EM algorithm. As specified in the NEMA NU-4 2008 protocol, the response function was formed by summing one-dimensional profiles that were parallel to the radial, tangential, and axial directions. A parabolic fit of the peak point and its two nearest neighboring points was used to determine the maximum value of the response function. Linear interpolation between adjacent pixels was used to determine the position of the half and one tenth of the parabolic curve maximum. The volumetric resolution was calculated on the basis of the FWHMs of the radial, tangential, and axial directions. While the NEMA NU-4 standards indicate that filtered back projection (FBP) should be used for the spatial resolution measurements, this was not possible here, since a FBP algorithm specific for the PETbox4 system with the unconventional geometry has not been developed. The main reason behind this is that the spatial sampling of the lines of response in the projection data, especially in the angular direction is highly non uniform due to the flat panel detector in close proximity geometry. As a result, the interpolations necessary for

resampling the data (including the estimated average DOI), would require a hybrid reconstruction based in part on Monte Carlo simulations, in combination with methods to fill in the missing data due to the gaps between the detector heads. Such a data reconstruction would also not comply with the NEMA NU-4 protocol and would be a unique feature to the particular geometry of PETbox4.

2.3.3. Sensitivity—Sensitivity is expressed as the fraction of the actual positron annihilation events that are detected as true coincidence events. A ^{68}Ge point-like source (Eckert & Ziegler Isotope Products, Valencia, CA) embedded in thin steel tubing was placed at the CFOV to measure the peak absolute sensitivity. The thin steel casing ensures annihilation of all the positrons, but does not cause significant attenuation of the 511 keV gamma rays. The activity of the point source was 21 kBq (0.56 μCi) measured in a calibrated well-type gamma counter (Wallac Wizard 1480, Perkin Elmer, Shelton, CT). The activity was low enough so that the counting losses were less than one percent and the randoms rate was less than 5% of the true event rate, fulfilling the NEMA NU 4–2008 protocol recommendations.

To investigate the sensitivity dependency on the energy threshold, the system peak absolute sensitivity measurements were acquired at the center of the FOV with a fixed upper-level discriminator (ULD) corresponding to 650 keV and a lower-level discriminator (LLD) corresponding to energies from 150 to 350 keV, in 50 keV steps. The axial sensitivity profile was measured with the same source stepped across the scanner from end to end of the axial FOV, with an energy window of 150–650 keV. The axial positions of the source were determined from the reconstructed images. The number of coincidences was recorded at each acquisition for 30 seconds. Delayed coincidences were subtracted from prompts before the true coincidences were divided by the actual source activity. This ratio was corrected for the branching ratio of ^{68}Ga (0.89), but the attenuation of the steel material surrounding the source was not compensated. The peak absolute sensitivity measurements were compared with simulated values obtained from GATE (Geant4 Application for Tomographic Emission) (Jan et al., 2004) simulations with the same configurations. The average sensitivity for a mouse-sized object (with a 7 cm axial length) was calculated from the measured axial sensitivity profile.

2.4. Scatter and count-rate performance

Count-rate performance was evaluated using the NEMA NU-4 mouse-sized phantom, which is a 70 mm long and 25mm diameter solid cylinder made of high density polyethylene (0.96 g/cm3), with a 3.2 mm diameter hole drilled parallel to the central axis at a radial offset of 10 mm. A flexible tube filled with ^{18}F solution was inserted into the 3.2 mm hole of the phantom. The initial activity was measured to be 2.52 MBq (68.2 μCi) using a dose calibrator (Atomlab 300; Biodex Medical Systems, Shirley, NY) at the start of the acquisition. The phantom was centered in the FOV and rotated by 45 degrees in order to achieve a more symmetric source distribution that is also a closer representation of the expected typical spatial distribution in mouse studies. An imaging chamber supporting the phantom was included in the FOV for this measurement, creating a realistic scatter

environment. Data were acquired until the total activity decayed below 10 kBq, while random coincidences were measured using the delayed window method.

The data was processed as specified by NEMA NU-4, briefly described here: In the prompts sinogram, the profile of direct projections from opposite crystals was shifted so that the peak pixels were aligned with the center pixel of the sinogram. A sum projection was produced by adding up all projections in each slice. All pixel counts outside of a 14-mm centered band were assumed to be due to the random and scatter counts. A linear interpolation between the left and right border of the 14 mm band was used to estimate these non-true counts under the profile peak. Counts above this line were taken as true events, while randoms were estimated from the delayed sinogram.

The scatter fraction was measured using a prompt sinogram with an activity of 74 kBq (2 μCi). This low activity frame was chosen to ensure that dead time and randoms did not affect the measurement. The scattered count rate was then calculated by Equation 1:

$$R_{scatter}=R_{prompt}-R_{true}-R_{random}, \quad (1)$$

where $R_{scatter}$, R_{prompt}, R_{true} and R_{random} are the scatter, prompt, true and random event rates, respectively. The scatter fraction (SF) was calculated by Equation 2:

$$SF=\frac{R_{scatter}}{R_{scatter}+R_{true}}, \quad (2)$$

The noise equivalent count rate (NECR) for each prompt sinogram was determined using the following equation:

$$NECR=\frac{R_{true}^2}{R_{prompt}+R_{random}}=\frac{(R_{prompt}-R_{random})^2\times(1-SF)^2}{R_{prompt}+R_{random}} \quad (3)$$

2.5. Imaging studies

2.5.1. NEMA phantom study—Image quality studies were performed using the image quality phantom described in the NEMA NU-4 protocol. The phantom (Data Spectrum Corporation, Hillsborough, NC) consists of the following three regions: a main fillable uniform region chamber allowing the uniformity to be measured; a lid that attaches to the main fillable region, containing 2 smaller cold region chambers (filled with water and air) that are used to quantify the spillover ratio (SOR); and a solid acrylic glass region with 5 fillable rods drilled through for measuring the recovery coefficients as a function of rod diameter. Since the PETbox4 is intended to be used with a low injection dose, the image-quality phantom was filled with 1.85 MBq (50 μCi) ^{18}F solution measured with a dose calibrator (Atomlab 300; Biodex Medical Systems, Shirley, NY). It should be pointed out that this activity is half the activity level recommended by the NEMA NU-4 protocol. The phantom was placed on a mouse imaging chamber to simulate actual mouse imaging and was imaged for 20 min, following the NEMA NU-4 recommendations. Normalization and random corrections were applied, but no scatter correction was applied. For attenuation

correction applied in this manuscript, a CT transmission scan of the object and its supporting bed was obtained using a MicroCAT II tomograph (Siemens Preclinical Solutions, Knoxville, TN). The reconstructed CT image was registered with the PET emission image and forward projected through the system response matrix to create an attenuation sinogram. The image was reconstructed by the ML-EM algorithm.

A 22.5-mm-diameter and 10-mm-high cylindrical volume of interest (VOI) was drawn over the center of the uniform region of the image-quality phantom. The average concentration values in this VOI, and standard deviation (SD) were measured to estimate the noise performance as a measure of uniformity. The image slices covering the central 10-mm length of the rods were averaged to obtain a single image slice of lower noise. Circular regions of interest (ROIs) were drawn in this image around each rod, with diameters twice the physical diameters of the rods. The maximum values in each of these ROIs were measured and divided by the mean value obtained in the uniformity test to obtain the recovery coefficient (RC) for each rod size. The transverse image pixel coordinates of the locations with the maximum ROI values were recorded and used to create 10 mm long line profiles along the rods in the axial direction. The SD of the pixel values measured along each line profile was calculated. Although no scatter correction was applied to the acquired dataset, the spillover ratios (SOR) of the water- and air-filled cold region chamber were calculated as specified in the NEMA NU-4 standard to provide a rough estimation of the scatter effects. The diameter of the VOI was 4 mm and encompassed the central 7.5 mm in length in the axial direction. The ratio of the mean in each cold region to the mean of the hot uniform area was reported as SOR.

2.5.2. Mouse study—A dynamic [^{18}F]-FDG study was performed on a healthy mouse to demonstrate the dynamic imaging capabilities of the PETbox4 system. The mouse was anesthetized with isoflurane, positioned in the imaging chamber, and placed in the PETbox4 system. At the beginning of a tail injection of 1.59 MBq (43 μCi) [^{18}F]-FDG, a 1 hour listmode file data acquisition was initiated. The data was sliced into 10 time frames, with lengths of 2, 2, 6, 50, 540, 600, 600, 600, 600 and 600 seconds. For each frame, volumetric images were reconstructed using the ML–EM method. Normalization and attenuation correction were applied, but no scatter correction was applied. VOIs were manually drawn for the bladder, heart and kidney in the reconstructed images. The mean image value in each VOI was calculated as a representation of the activity distribution in that organ. To validate system performance with isotopes other than ^{18}F, a static study with an antibody fragment radiolableled with ^{64}Cu was performed. A healthy mouse was injected with ^{64}Cu radiolabeled minibody and after an uptake of 4 hours, the mouse was scanned for 20 min. The activity was 0.14 MBq (3.7 μCi) in the entire mouse at scan time. To demonstrate the imaging capabilities of the PETbox4/MARS system, MARS scans were performed after the PET acquisition. The x-ray source configuration was set at 40 kVp, 100 μA, and 3 sec exposure. The camera exposure time for the optical photographic image was set to 200 ms.

3. Results

3.1. Energy resolution and Flood Histograms

Figure 3 (a) shows the flood histogram taken from one of the detector panels. In the flood histograms from the four detectors, more than 95% of the individual crystal elements in the 24 × 50 array are clearly identified. Table 2 summarizes the measured energy resolution for the four detector panels. For the crystals in the four panels, the measured crystal energy resolution ranged from 14% to 48% FWHM, with a mean of 18%. Figure 3 (b) shows a vertical profile across one column of crystals in the flood histogram, and figure 3 (c) shows a horizontal profile across one row. Although the edge crystals are not very well resolved, most of the other crystals have a good peak to valley separation (average 3.55). Figure 4 shows the non-uniformity of the energy resolution across all crystals in one detector panel and representative energy spectra of two individual crystals at different locations of the detector. It was observed that crystals at the center of each PSPMT tend to yield better energy resolution than edge crystals or crystals at the junction of the two PSPMTs.

In contrast, the prototype PETbox had an average energy resolution of 20%, despite the lower aspect ratio of its individual crystal elements. The improvement of the energy resolution is believed to be largely the result of the high quality reflector film around each pixel in the PETbox4 detector module resulting in better light collection efficiency. The detector blocks on the PETbox were left as cut, without any reflector between the individual pixels. Also, the addition of reflector between the individual pixels helps to reduce the light spread in the PMT, leading to the collection of light from a smaller and more uniform area of the PMT photocathode, potentially leading to improved energy resolution.

3.2. Spatial resolution

3.2.1. Intrinsic spatial resolution—The intrinsic spatial resolution of an opposing detector pair is shown in figure 5. For crystal pairs along the detector short axis, the measured FWHM ranged from 1.40 mm to 1.67 mm, with an average value of 1.51 mm. For crystal pairs along the detector long axis, the measured FWHM ranged from 1.34 mm to 1.64 mm, with an average value of 1.49 mm. In contrast, the previous prototype PETbox had an intrinsic spatial resolution ranging from 1.48 to 2.39 mm, with an average of 1.78 mm.

3.2.2. Image spatial resolution—Figure 6 (a) and (b) show the image spatial resolution in the radial, tangential, and axial directions measured in the central and 1/4 axial transverse plane in compliance with the NEMA NU-4 standard, respectively. The resolution in each of three orthogonal directions is below 2 mm FWHM and rather uniform, with an isotropic mean value of 1.5 mm FWHM.

The volumetric resolution, defined as the product of all three image resolution components of a system, is shown in figure 6 (c) and compared with that of the prototype PETbox. The improvement of the PETbox4 over the PETbox ranges from 1.2-fold at the CFOV (3.4 μL vs. 4.1 μL) to 2.6-fold at 1.5 cm radial offset (2.6 μL vs. 6.7 μL). At a 23.5-mm axial offset, the improvement ranges from 2-fold at the center of the transverse plane (2.7 μL vs. 5.3 μL) to 2.1-fold at 1.5 cm radial offset (3.6 μL vs. 7.4 μL).

3.3. Sensitivity

Figure 7 summarizes the peak system sensitivity at the CFOV for different energy window settings. As the energy window changes from 350–650 keV to 150–650 keV, the peak system sensitivity varies from 9.3% to 18.1%. With the default energy window of 150–650 keV, the PETbox4 has a peak system sensitivity of 18.1%, a fourfold improvement over the prototype PETbox at the same energy window. The measurements were in close agreement with the sensitivity estimated with the GATE simulation. The axial sensitivity profile is shown in figure 8. The PETbox4 system employs a closely packed geometry which leads to an increased fraction of backscatter events included in the coincidence timing window, therefore the sensitivity did not immediately decrease to zero when the source was stepped out of the axial FOV. The average sensitivity for a mouse-sized object (7 cm axial length) is 14% with an energy window of 150–650 keV.

3.4. Scatter and count-rate performance

Figure 9(a) illustrates the experimental setup for the count rate performance measurement. The phantom was centered in the FOV and rotated by 45 degrees. The prompt, random and NEC rates as a function of total activity in the mouse-sized phantom are plotted in figure 9(b). With the default energy window of 150–650 keV and timing window of 20 ns, the prompt rates reach peak values at around 1.7 MBq (45 μCi) total activity. With this activity, the random events account for approximately 3% of the total prompt counts. The PETbox4 system has a coincidence timing resolution of 4 ns FWHM, but since the random rate is low, a large timing window of 20 ns is used to increase the system sensitivity. This way, a number of prompt events that fall on the coincidence spectrum tails are accepted, and this done for all the measurements presented in this report. The peak NECR is 35kcps achieved at a total activity of 1.5 MBq (40 μCi) in the phantom. The scatter fraction at this acquisition setting is 28%, which is mainly due to the bed support, the gantry material around the detectors, as well as the detector material itself.

3.5. Imaging studies

3.5.1. Phantom studies—Figure 10 shows the images of a transverse plane of the uniform region (figure 10(a)), a transverse plane with 5 rods (figure 10(b)), a coronal plane (figure 10(c)), and a profile across the uniform area (figure 10(d)) of the NEMA NU-4 image-quality phantom. With the ML-EM reconstruction, the SD in the uniform region was 5.7%. The RCs for 5 different rod sizes from 1- to 5-mm diameter are shown in figure 11. The RC for the smallest 1-mm rod is 0.10, and for the largest 5-mm rod the RC is 0.87. The RCs measured in the first generation PETbox system (Zhang et al., 2011) are also shown in figure 11 for comparison.

The SOR measured in the water- and air-filled cold region chamber were calculated to be 14.7% and 13.3%, respectively. Since no scatter correction was applied for the acquired dataset, the SOR are indicative of the effect of scattered radiation on the reconstructed images.

In vivo mouse studies—Figure 12 shows selected reconstructed average intensity projection (AIP) images from eight frames corresponding to the time period: (a) 0–2 s, (b)

2–4 s, (c) 4–10 s, (d) 10–60 s, (e) 1–10 min, (f) 10–20 min, (g) 20–30 min, and (h) 50–60 min following the injection in the dynamic [^{18}F]-FDG study. The reconstructed images show the tail injection in early frames and the activity building up in the lungs, kidney, liver, bladder, and heart in later frames. The measured time–activity curves for the bladder, heart, and kidney are plotted in figure 13, which clearly reveals the trend of activity distribution in these organs as time progresses. Figure 14 shows the reconstructed coronal, sagittal and transverse slices from the last 10 min frame of the same study. The activity in the entire mouse was 0.93 MBq (25 μCi) at scan time. Figure 15 illustrates the capabilities of the PETbox4/MARS combination system. In this static 20 minute ^{64}Cu study, a reconstructed three-dimensional volume PET image was registered with the MARS data set to provide an anatomical reference (Wang et al., 2011; Wang et al., 2012). The activity in the entire mouse was 0.14 MBq (3.7 μCi) at scan time. (A video clip can be accessed online as the supplementary data enhancement.)

4. Discussion

This study has evaluated the overall performance of the PETbox4 system according to NEMA NU-4 standards with some modifications as necessary.

Compared to the first generation PETbox system, PETbox4 employs different crystal-cutting technology that reduces the gaps between adjacent crystals from 200 to 78 microns. The new detector block provides a higher packing fraction of 0.92 compared to 0.83 of the previous generation detectors. With the help of the reflectors between individual pixels used in PETbox4 detectors, the scintillation light collection is improved and the light cross talk between neighbor crystals is suppressed, allowing the use of crystals with smaller cross section and higher aspect ratio. The energy resolution and the average intrinsic spatial resolution of the PETbox4 detector are thus improved to 18% and 1.5 mm FWHM, compared with 20% and 1.8 mm FWHM for that of the PETbox detector, respectively.

With an energy window of 150–650 keV and a timing window of 20 ns, the system peak absolute sensitivity of the PETbox4 reaches 18% at the center of the FOV, a more than four-fold improvement relative to the first generation PETbox system. The significant sensitivity enhancement is due to the more than three-fold detection solid angle increase by doubling the number of detectors modules from 2 to 4, and allowing coincidences between all possible detector head combinations. Also, the increased thickness of each detector block from 5 mm to 7 mm, and the improved crystal packing fraction from 0.83 to 0.92, contribute further to the sensitivity increase, which should be of benefit in the investigation of biological processes in small animals. The small discrepancy between the Monte Carlo simulations and the measured data is most likely due to differences in the spatial distribution and magnitude of the detector energy resolution. But these results reconfirm the accuracy of the GATE model for estimating the performance parameters of PET systems.

Despite the fact that the detection of coincidences along very oblique angles are allowed owing to the close geometry of the scanner, the ML-EM reconstruction accurately models the physical response of the scanner in the system matrix. As a result, the spatial resolution is fairly homogeneous within the entire FOV and averages at 1.5 mm FWHM with an

average volumetric resolution of 3 μL, allowing the investigation of whole-body biodistribution studies of mice without degradation of the spatial resolution toward the edges of the FOV. The significantly improved uniformity of the image spatial resolution arises mainly from improved data sampling along the anterior-posterior direction by employing two side detectors in the PETbox4 system. The lack of these data was the main source of volumetric resolution degradation at large offsets from the center for the two head PETbox. It is worth to also note here that for the flat panel geometries of the detectors used in both systems, depth of interaction parallax effects for coincidence lines of response are minimal at the edges of the detectors rather than at their center. We also need to stress again that the reconstruction method utilized here deviates significantly from the NEMA NU-4 protocol, because the traditional FBP reconstruction was not available for the PETbox4 geometry. We anticipate that the development of other PET preclinical instruments with geometries that are more radically different from cylindrical ring tradition (Goorden et al., 2013) for which also FBP is not possible, indicates that the NEMA NU-4 standards need to be revisited. Nevertheless, the absolute measurements of resolution with a point source in air and an iterative reconstruction algorithm need to be taken with an air of caution. In vivo images of mouse subjects with distributed sources and background demonstrate that the system is capable of acquiring data and reconstructing high quality images.

Following the NEMA standard, the count rate performance of the PETbox4 has been measured with a mouse sized cylindrical phantom. The phantom was rotated by 45 degrees to achieve a more symmetric source distribution. However, even with this approach, it is still difficult to compare between PETbox4 and PETbox. For the PETbox, the phantom was placed in the system so that the line source was located at the midway between the two opposing detectors to ensure that the dead time experienced by the two detector heads were similar. For the PETbox4 system, the 1 cm offset line source was much closer to two of the four detector panels. Therefore saturation of the system was dominated by the dead time of these two heads, leading to an underestimated count rate performance compared to a more symmetric activity distribution, such as the image quality phantom study and typical in-vivo mouse imaging. With this source geometry, the peak NECR is 35 kcps (achieved at 1.5 MBq). The higher sensitivity of the PETbox4 is such that the peak NECR is reached at lower total activity for this scanner. The overall count rate performance is mainly limited by the highly multiplexed detector readouts (four signals for groups of 1200 crystals) and the slow decay time of the BGO scintillation light. In the future, the count rate performance for the same scintillator can be greatly improved by developing a less multiplexed readout. For the current system, a pulse pile-up rejection and correction method has been implemented for all the data shown here, details of which will be presented elsewhere.

The choice for the 1 cm radial offset of the line source in the NEMA mouse sized phantom was dictated by Monte Carlo simulations performed to determine the line source position which gave a scatter fraction similar to that found in a uniformly filled cylindrical phantom of the same size (Surti et al., 2005). For scanners with close geometry, a 1 cm offset of the line source is relatively large difference compared to the radioactivity biodistribution in a typical in-vivo mouse acquisition. This difference may cause earlier saturation of detectors closer to the line source and an underestimation of the system count rate performance. The NEMA NU-4 evaluation also strongly depends on the orientation of the phantom, thus

making comparisons between systems difficult. Moreover, for scanners with less sensitivity or better count rate performance, high level radioactivity concentration is required to fill the small volume of the line source in order to saturate the system. This approach increases the difficulty of filling the phantom and the dose to the personnel and therefore this is something that we recommend that should be revisited in a possible update to the NEMA standards.

Nevertheless, it is true that the overall peak NEC rate for both PETbox systems is much lower than the peak NEC rate for most other preclinical PET instruments. Even though this performance parameter is interesting, it does not play a significant role under realistic mouse imaging scenarios. The peak NEC rates for most existing preclinical imaging instruments are achieved at mouse phantom activities around (50–200 MBq) (Goertzen et al., 2012). These total activities at peak NEC are 5–20 times larger than the 7.4 MBq doses typically used today for mouse studies with any preclinical PET system. This typical injected dose is itself 60 times more concentrated than the typical human PET injected dose (296 kBq/g versus 5 kBq/g respectively). The main reason is that the average 25 g mouse weighs approximately 3000 times less than the average human. Consequently the design goal of the PETbox4 system has been high sensitivity imaging of mice at low dose. The typical injected dose of 1 MBq for studies with the PETbox4 system is seven times smaller than the dose considered standard in the field, a dose established with systems of very different design and capabilities (Chatziioannou et al., 1999). For this reason also the NEMA NU-4 mouse image quality phantom in this work was filled with only half the recommended activity, but scanned for the recommended 20 minute duration.

Data management can also become an issue in transferring and archiving studies. The PETbox4 system outputs 32-Bit list mode data, half size compared to the previous prototype PETbox system (64-Bit) due to the online crystal and energy discriminations implemented in FPGA with the LUT stored in the SDRAM on the VHS-ADC board. This doubles the data transmission bandwidth in the list mode stream and provides more flexibility for future system development.

The current default energy window is set to be 150–650 keV. Due to the more closely packed system geometry, an increased fraction of backscatter events are included in the coincidence timing window (Goertzen et al., 2010), which degrade the signal-to-noise ratio of the final image. On the other hand, events that undergo a single Compton interaction in the BGO crystals but still describe the correct line of response should be accepted. Therefore the optimization of energy window in a way that balances these two effects is now under investigation. Scatter correction techniques have not yet been explored or implemented. Future research will also be devoted to implementing adequate scatter correction methodology and evaluations on performing quantitative studies using this system. The MDA, as a combination of the more traditional PET system parameters, represents the performance of a PET scanner at very low activity distributions and is directly related to lesion detection (Bao and Chatziioannou, 2010). Novel molecular imaging applications, such as cell trafficking studies (Adonai et al., 2002) or gene expression imaging (Blasberg, 2002), have brought the need to image small and low activity sources on the order of nano Curies under low contrast conditions. The PETbox4 system, with its high sensitivity and low intrinsic background, should achieve good MDA performance. A comprehensive evaluation

of MDA for PETbox4 will be performed and compared with other systems in future work. Although further improvements are foreseen in the near future for the prototype scanner we have presented in this work, this design has been implemented by Sofie Biosciences (Culver City, CA) into a commercial scanner, GENISYS4.

5. Conclusion

In conclusion, this study has evaluated the basic performance of the PETbox4 system and its improvement over the previous system. Our results indicate a significant improvement in nearly all aspects of typical PET system characteristics compared with the first generation PETbox system. The energy resolution of the PETbox4 system averages 18% for the 511 keV photopeak. The volumetric image resolution remains around 3 μL within the central 4-cm diameter FOV and is uniform along the radial, transverse and axial directions through the whole FOV. The peak sensitivity is 18% with a 150– 650 keV energy window and a 20 ns timing window. The peak NEC rate is 35 kcps achieved at a total activity of 1.5 MBq (40 μCi). The selected animal studies show that the system is capable of static and dynamic mouse imaging studies with different radiotracers. The overall performance demonstrates that the PETbox4 scanner is suitable for producing high quality images for molecular imaging based biomedical research, with less administered activity and lower dose delivered to the mice. At the same time, the cost derived from detectors and electronics as well as the system overall footprint is significantly reduced in this design compared with a more conventional ring-based preclinical PET tomographs.

Supplementary Material

Refer to Web version on PubMed Central for supplementary material.

Acknowledgments

The authors would like to thank the staff of the Crump Imaging facility at UCLA including Waldemar Ladno, Darin Williams, and Jeffrey Collins for their assistance with obtaining the ^{18}F solution for this study. This work was supported by the National Institutes of Health under grant no. R24 CA92865, the Department of Energy under contract no. DE-FG02-06ER64249, and the UCLA Foundation from a donation made by Ralph and Marjorie Crump for the UCLA Crump Institute for Molecular Imaging.

References

Adonai N, Nguyen KN, Walsh J, Iyer M, Toyokuni T, Phelps ME, McCarthy T, McCarthy DW, Gambhir SS. Ex vivo cell labeling with Cu-64-pyruvaldehyde-bis(N-4-methylthiosemicarbazone) for imaging cell trafficking in mice with positron-emission tomography. P Natl Acad Sci USA. 2002; 99:3030–3035.

Amundson SA, Bittner M, Meltzer P, Trent J, Fornace AJ. Induction of gene expression as a monitor of exposure to ionizing radiation. Radiat Res. 2001; 156:657–661. [PubMed: 11604088]

Bao, Q.; Chatziioannou, AF. GATE simulation of a BGO based high sensitivity small animal PET scanner; Noninvasive Functional Source Imaging of the Brain and Heart & inter. Conf. Funcational Biomedical Imaging; 2007. p. 47-50.

Bao Q, Newport D, Chen M, Stout DB, Chatziioannou AF. Performance Evaluation of the Inveon Dedicated PET Preclinical Tomograph Based on the NEMA NU-4 Standards. J Nucl Med. 2009; 50:401–408. [PubMed: 19223424]

Bao QN, Chatziioannou AF. Estimation of the minimum detectable activity of preclinical PET imaging systems with an analytical method. Med Phys. 2010; 37:6070–6083. [PubMed: 21158319]

Bergeron M, Cadorette J, Beaudoin JF, Lepage MD, Robert G, Selivanov V, Tetrault MA, Viscogliosi N, Norenberg JP, Fontaine R, Lecomte R. Performance Evaluation of the LabPET APD-Based Digital PET Scanner. Ieee T Nucl Sci. 2009; 56:10–16.

Blasberg R. PET imaging of gene expression. Eur J Cancer. 2002; 38:2137–2146. [PubMed: 12387839]

Bloomfield PM, Rajeswaran S, Spinks TJ, Hume SP, Myers R, Ashworth S, Clifford KM, Jones WF, Byars LG, Young J, Andreaco M, Williams CW, Lammertsma AA, Jones T. The Design and Physical Characteristics of a Small Animal Positron Emission Tomograph. Physics in Medicine and Biology. 1995; 40:1105–1126. [PubMed: 7659733]

Canadas M, Embid M, Lage E, Desco M, Vaquero JJ, Perez JM. NEMA NU 4–2008 Performance Measurements of Two Commercial Small-Animal PET Scanners: ClearPET and rPET-1. Ieee T Nucl Sci. 2011; 58:58–65.

Chatziioannou AF. Molecular imaging of small animals with dedicated PET tomographs. Eur J Nucl Med. 2002a; 29:98–114.

Chatziioannou AF. PET scanners dedicated to molecular imaging of small animal models. Mol Imaging Biol. 2002b; 4:47–63. [PubMed: 14538048]

Chatziioannou AF, Cherry SR, Shao YP, Silverman RW, Meadors K, Farquhar TH, Pedarsani M, Phelps ME. Performance evaluation of microPET: A high-resolution lutetium oxyorthosilicate PET scanner for animal imaging. J Nucl Med. 1999; 40:1164–1175. [PubMed: 10405138]

Cherry SR, Shao Y, Silverman RW, Meadors K, Siegel S, Chatziioannou A, Young JW, Jones WF, Moyers JC, Newport D, Boutefnouchet A, Farquhar TH, Andreaco M, Paulus MJ, Binkley DM, Nutt R, Phelps ME. MicroPET: A high resolution PET scanner for imaging small animals. Ieee T Nucl Sci. 1997; 44:1161–1166.

Correia JA, Burnham CA, Kaufman D, Brownell AL, Fischman AJ. Performance evaluation of MMP-II: A second-generation small animal PET. Ieee T Nucl Sci. 2004; 51:21–26.

de Jong HWAM, van Velden FHP, Kloet RW, Buijs FL, Boellaard R, Lammertsma AA. Performance evaluation of the ECAT HRRT: an LSO-LYSO double layer high resolution, high sensitivity scanner. Physics in Medicine and Biology. 2007; 52:1505–1526. [PubMed: 17301468]

de Marcillac P, Coron N, Dambier G, Leblanc J, Moalic JP. Experimental detection of alpha-particles from the radioactive decay of natural bismuth. Nature. 2003; 422:876–878. [PubMed: 12712201]

Di Domenico G, Zavattini G, Moretti E, Piffanelli A, Giganti M, Motta A, Sabba N, Uccelli L, Benini E, Duatti A, Bolzati C, Boschi A, Del Guerra A. YAP-(S)PET small animal scanner: Quantitative results. Ieee T Nucl Sci. 2003; 50:1351–1356.

Funk T, Sun M, Hasegawa BH. Radiation dose estimate in small animal SPECT and PET. Med Phys. 2004; 31:2680–2686. [PubMed: 15487751]

Gagnon MKJ, Hausner SH, Marik J, Abbey CK, Marshall JF, Sutcliffe JL. High-throughput in vivo screening of targeted molecular imaging agents. P Natl Acad Sci USA. 2009; 106:17904–17909.

Gambhir SS. Molecular imaging of cancer with positron emission tomography. Nat Rev Cancer. 2002; 2:683–693. [PubMed: 12209157]

Goertzen AL, Bao QN, Bergeron M, Blankemeyer E, Blinder S, Canadas M, Chatziioannou AF, Dinelle K, Elhami E, Jans HS, Lage E, Lecomte R, Sossi V, Surti S, Tai YC, Vaquero JJ, Vicente E, Williams DA, Laforest R. NEMA NU 4–2008 Comparison of Preclinical PET Imaging Systems. J Nucl Med. 2012; 53:1300–1309. [PubMed: 22699999]

Goertzen AL, Stout DB, Thompson CJ. A method for measuring the energy spectrum of coincidence events in positron emission tomography. Physics in Medicine and Biology. 2010; 55:535–549. [PubMed: 20023324]

Goertzen AL, Suk JY, Thompson CJ. Imaging of weak-source distributions in LSO-based small-animal PET scanners. J Nucl Med. 2007; 48:1692–1698. [PubMed: 17873140]

Goorden MC, van der Have F, Kreuger R, Ramakers RM, Vastenhouw B, Burbach JP, Booij J, Molthoff CF, Beekman FJ. VECTor: a preclinical imaging system for simultaneous submillimeter SPECT and PET. J Nucl Med. 2013; 54:306–312. [PubMed: 23077113]

Huisman MC, Reder S, Weber AW, Ziegler SI, Schwaiger M. Performance evaluation of the Philips MOSAIC small animal PET scanner. Eur J Nucl Med Mol I. 2007; 34:532–540.

Hume SP, Gunn RN, Jones T. Pharmacological constraints associated with positron emission tomographic scanning of small laboratory animals. Eur J Nucl Med. 1998; 25:173–176. [PubMed: 9473266]

Jan S, Santin G, Strul D, Staelens S, Assie K, Autret D, Avner S, Barbier R, Bardies M, Bloomfield PM, Brasse D, Breton V, Bruyndonckx P, Buvat I, Chatziioannou AF, Choi Y, Chung YH, Comtat C, Donnarieix D, Ferrer L, Glick SJ, Groiselle CJ, Guez D, Honore PF, Kerhoas-Cavata S, Kirov AS, Kohli V, Koole M, Krieguer M, van der Laan DJ, Lamare F, Largeron G, Lartizien C, Lazaro D, Maas MC, Maigne L, Mayet F, Melot F, Merheb C, Pennacchio E, Perez J, Pietrzyk U, Rannou FR, Rey M, Schaart DR, Schmidtlein CR, Simon L, Song TY, Vieira JM, Visvikis D, de Walle RV, Wieers E, Morel C. GATE: a simulation toolkit for PET and SPECT. Physics in Medicine and Biology. 2004; 49:4543–4561. [PubMed: 15552416]

Jeavons AP, Chandler RA, Dettmar CAR. A 3D HIDAC-PET camera with sub-millimetre resolution for imaging small animals. Ieee T Nucl Sci. 1999; 46:468–473.

Knoess C, Siegel S, Smith A, Newport D, Richerzhagen N, Winkeler A, Jacobs A, Goble RN, Graf R, Wienhard K, Heiss WD. Performance evaluation of the microPET R4 PET scanner for rodents. Eur J Nucl Med Mol Imaging. 2003; 30:737–747. [PubMed: 12536244]

Laforest R, Longford D, Siegel S, Newport DF, Yap J. Performance evaluation of the microPET (R) - FOCUS-F120. Ieee T Nucl Sci. 2007; 54:42–49.

Lage E, Vaquero JJ, Sisniega A, Espana S, Tapias G, Abella M, Rodriguez-Ruano A, Ortuno JE, Udias A, Desco M. Design and performance evaluation of a coplanar multimodality scanner for rodent imaging. Physics in Medicine and Biology. 2009; 54:5427–5441. [PubMed: 19700817]

Lecomte R, Cadorette J, Rodrigue S, Lapointe D, Rouleau D, Bentourkia M, Yao R, Msaki P. Initial results from the Sherbrooke avalanche photodiode positron tomograph. Ieee T Nucl Sci. 1996; 43:1952–1957.

Li HD, Wong WH, Baghaei H, Uribe J, Wang Y, Zhang YX, Kim SS, Ramirez R, Liu JG, Liu ST. The engineering and initial results of a transformable low-cost high-resolution PET camera. Ieee T Nucl Sci. 2007; 54:1583–1588.

Malakoff D. The rise of the mouse, biomedicine's model mammal. Science. 2000; 288:248. −+ [PubMed: 10777401]

Marshall E. Genome sequencing - Celera assembles mouse genome; Public labs plan new strategy. Science. 2001; 292:822–823. [PubMed: 11341257]

Miyaoka RS, Janes ML, Lee K, Park B, Kinahan PE, Lewellen TK. Development of a single detector ring micro crystal element scanner: QuickPET II. Mol Imaging. 2005; 4:117–127. [PubMed: 16105510]

Mumcuoglu EU, Leahy R, Cherry SR, Zhou ZY. Fast Gradient-Based Methods for Bayesian Reconstruction of Transmission and Emission Pet Images. Ieee T Med Imaging. 1994; 13:687–701.

Myers R. The biological application of small animal PET imaging. Nucl Med Biol. 2001; 28:585–593. [PubMed: 11516702]

Paigen K. A miracle enough: the power of mice. Nat Med. 1995; 1:215–220. [PubMed: 7585036]

Phelps ME. Positron emission tomography provides molecular imaging of biological processes. P Natl Acad Sci USA. 2000; 97:9226–9233.

Prasad R, Ratib O, Zaidi H. Performance Evaluation of the FLEX Triumph X-PET Scanner Using the National Electrical Manufacturers Association NU-4 Standards. J Nucl Med. 2010; 51:1608–1615. [PubMed: 20847182]

Prasad R, Ratib O, Zaidi H. NEMA NU-04-based performance characteristics of the LabPET-8, (TM) small animal PET scanner. Physics in Medicine and Biology. 2011; 56:6649–6664. [PubMed: 21941029]

Rouze NC, Schmand M, Siegel S, Hutchins GD. Design of a small animal PET imaging system with 1 microliter volume resolution. Ieee T Nucl Sci. 2004; 51:757–763.

Sanchez F, Moliner L, Correcher C, Gonzalez A, Orero A, Carles M, Soriano A, Rodriguez-Alvarez MJ, Medina LA, Mora F, Benlloch JM. Small animal PET scanner based on monolithic LYSO crystals: Performance evaluation. Medical Physics. 2012; 39:643–653. [PubMed: 22320773]

Schafers KP, Reader AJ, Kriens M, Knoess C, Schober O, Schafers M. Performance evaluation of the 32-module quadHIDAC small-animal PET scanner. J Nucl Med. 2005; 46:996–1004. [PubMed: 15937311]

Seidel J, Vaquero JJ, Green MV. Resolution uniformity and sensitivity of the NIH ATLAS small animal PET scanner: Comparison to simulated LSO scanners without depth-of-interaction capability. Ieee T Nucl Sci. 2003; 50:1347–1350.

Surti S, Karp JS, Perkins AE, Cardi CA, Daube-Witherspoon ME, Kuhn A, Muehllehner G. Imaging performance of A-PET: A small animal PET camera. Ieee T Med Imaging. 2005; 24:844–852.

Surti S, Karp JS, Perkins AE, Freifelder R, Muehllehner G. Design evaluation of A-PET: A high sensitivity animal PET camera. Ieee T Nucl Sci. 2003; 50:1357–1363.

Szanda I, Mackewn J, Patay G, Major P, Sunassee K, Mullen GE, Nemeth G, Haemisch Y, Blower PJ, Marsden PK. National Electrical Manufacturers Association NU-4 Performance Evaluation of the PET Component of the NanoPET/CT Preclinical PET/CT Scanner. J Nucl Med. 2011; 52:1741–1747. [PubMed: 21969357]

Tai YC, Chatziioannou A, Siegel S, Young J, Newport D, Goble RN, Nutt RE, Cherry SR. Performance evaluation of the microPET P4: a PET system dedicated to animal imaging. Physics in Medicine and Biology. 2001; 46:1845–1862. [PubMed: 11474929]

Tai YC, Chatziioannou AF, Yang YF, Silverman RW, Meadors K, Siegel S, Newport DF, Stickel JR, Cherry SR. MicroPET II: design, development and initial performance of an improved microPET scanner for small-animal imaging. Physics in Medicine and Biology. 2003; 48:1519–1537. [PubMed: 12817935]

Tai YC, Ruangma A, Rowland D, Siegel S, Newport DF, Chow PL, Laforest R. Performance evaluation of the microPET focus: A third-generation microPET scanner dedicated to animal imaging. J Nucl Med. 2005; 46:455–463. [PubMed: 15750159]

Taschereau R, Chatziioannou AF. Monte Carlo simulations of absorbed dose in a mouse phantom from 18-fluorine compounds. Med Phys. 2007; 34:1026–1036. [PubMed: 17441249]

Taschereau, R.; Rannou, FR.; Chatziioannou, AF. A Modeled Point Spread Function For a Noise-Free System Matrix; IEEE NSS/MIC 2011 Conf. Record; 2011. p. 4102-4105.

Wang GJ, Cai L. Induction of cell-proliferation hormesis and cell-survival adaptive response in mouse hematopoietic cells by whole-body low-dose radiation. Toxicol Sci. 2000; 53:369–376. [PubMed: 10696785]

Wang H, Stout DB, Chatziioannou AF. Mouse Atlas Registration with Non-tomographic Imaging Modalities-a Pilot Study Based on Simulation. Molecular Imaging and Biology. 2011; 14:408–419. [PubMed: 21983855]

Wang HK, Stout DB, Taschereau R, Gu Z, Vu NT, Prout DL, Chatziioannou AF. MARS: a mouse atlas registration system based on a planar x-ray projector and an optical camera. Physics in Medicine and Biology. 2012; 57:6063–6077. [PubMed: 22968224]

Wang YC, Seidel J, Tsui BMW, Vaquero JJ, Pomper MG. Performance evaluation of the GE healthcare eXplore VISTA dual-ring small-animal PET scanner. J Nucl Med. 2006; 47:1891–1900. [PubMed: 17079824]

Weber S, Bauer A, Herzog H, Kehren F, Muhlensiepen H, Vogelbruch J, Coenen HH, Zilles K, Halling H. Recent results of the TierPET scanner. Ieee T Nucl Sci. 2000; 47:1665–1669.

Weissleder R, Mahmood U. Molecular imaging. Radiology. 2001; 219:316–333. [PubMed: 11323453]

Yonezawa M. Induction of radio-resistance by low dose X-irradiation. Yakugaku Zasshi. 2006; 126:833–840. [PubMed: 17016014]

Zhang H, Bao QA, Vu NT, Silverman RW, Taschereau R, Berry-Pusey BN, Douraghy A, Rannou FR, Stout DB, Chatziioannou AF. Performance Evaluation of PETbox: A Low Cost Bench Top Preclinical PET Scanner. Mol Imaging Biol. 2011; 13:949–961. [PubMed: 20812031]

Zhang H, Vu NT, Bao Q, Silverman RW, Berry-Pusey BN, Douraghy A, Williams DA, Rannou FR, Stout DB, Chatziioannou AF. Performance Characteristics of BGO Detectors for a Low Cost Preclinical PET Scanner. Ieee T Nucl Sci. 2010; 57:1038–1044.

Ziemons K, Auffray E, Barbier R, Brandenburg G, Bruyndonckx P, Choi Y, Christ D, Costes N, Declais Y, Devroede O, Dujardin C, Fedorovd A, Heinrichs U, Korjik M, Krieguer M, Kuntner C, Largeron G, Lartizien C, Larue H, Lecoq P, Leonard S, Marteau J, Morel C, Mosset JB, Parl C,

Pedrini C, Petrosyan AG, Pietrzyk U, Rey M, Saladino S, Sappey-Marinier D, Simon L, Streun M, Tavernier S, Vieira JM. The ClearPET (TM) project: development of a 2nd generation high-performance small animal PET scanner. Nucl Instrum Meth A. 2005; 537:307–311.

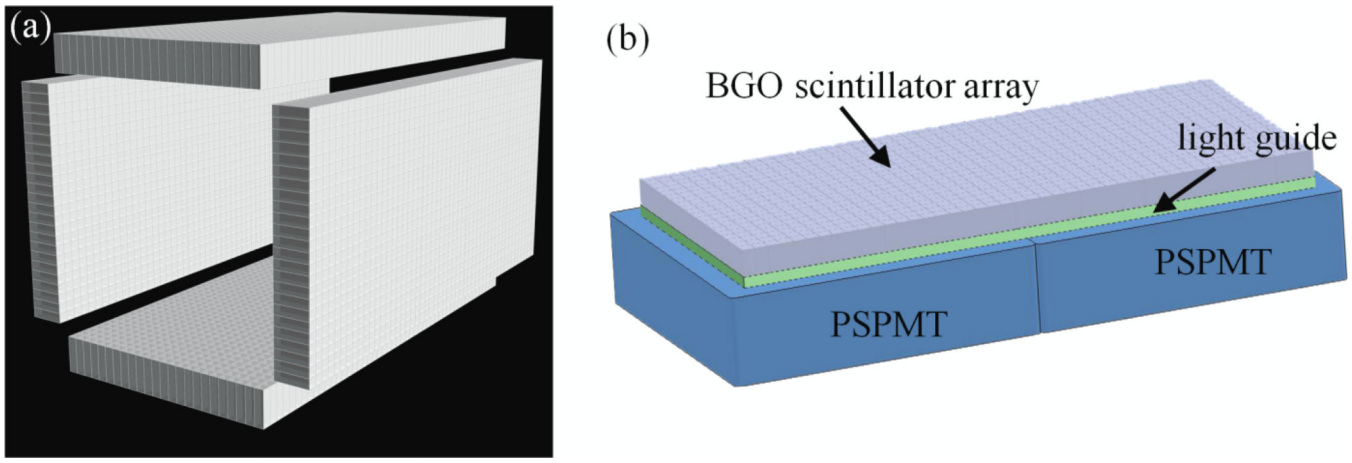

Figure 1.

(a) PETbox4 system detector configuration. Four detectors are arranged in a box like geometry, with a spacing of 5cm between opposing detector panels. (b) Schematic drawing of a PETbox4 detector module. The complete detector module employs two H8500 PMTs to detect scintillation light from a 24 × 50 BGO crystal array.

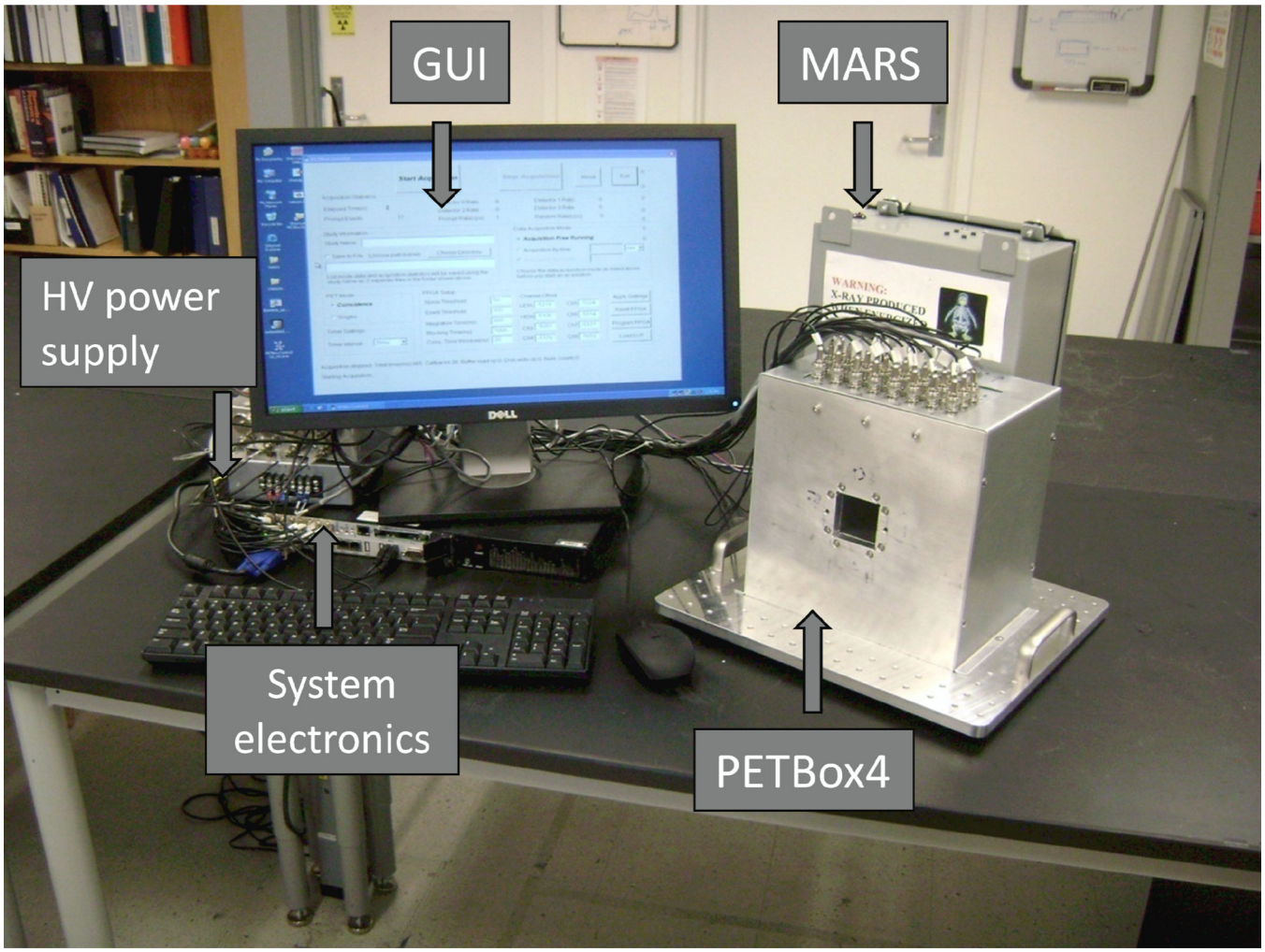

Figure 2.

A photogragh of the entir PETbox4 system, including the MARS, the data acq quisition electronics and the controlling computer.

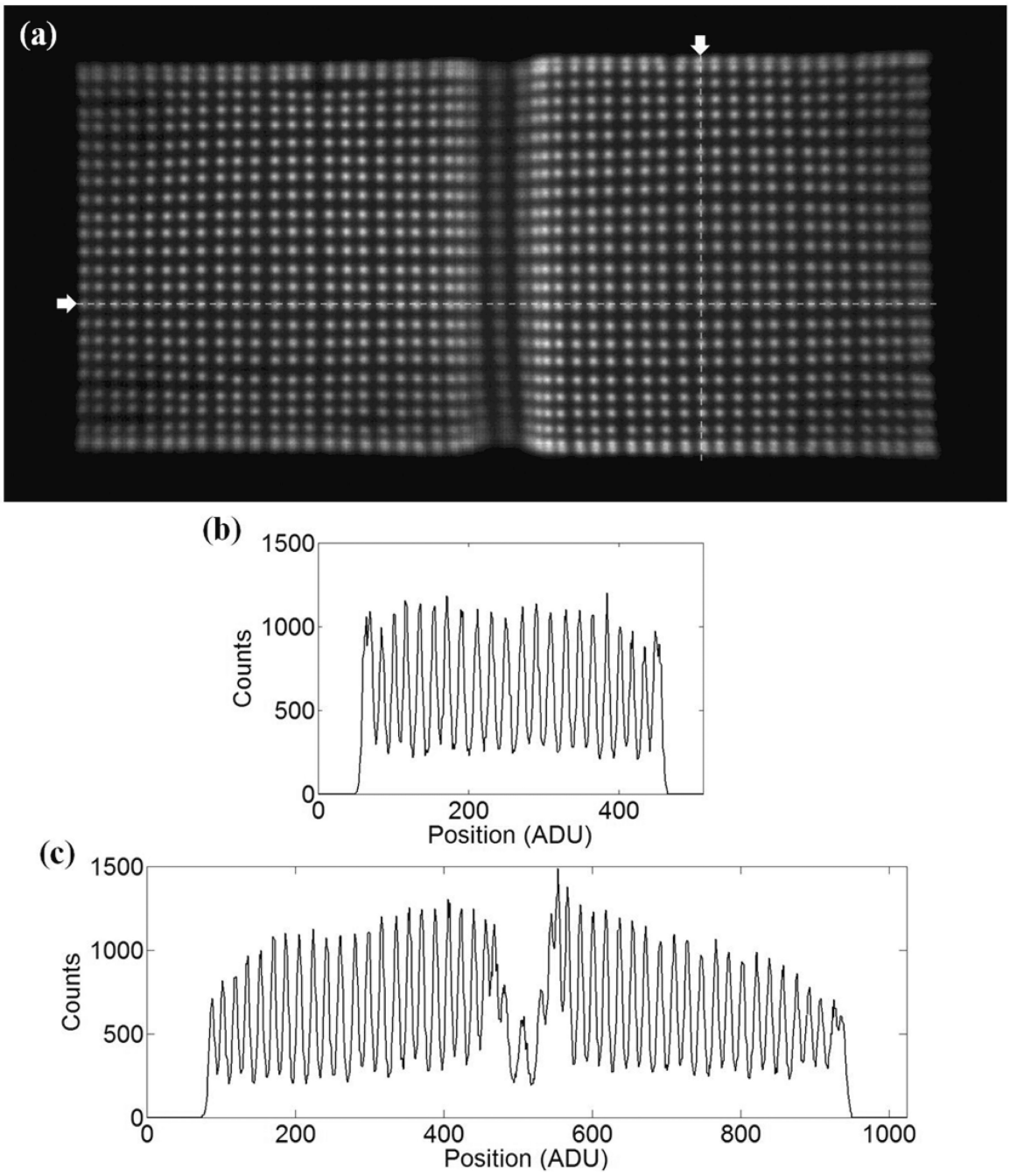

Figure 3.

(a) Flood image taken from one of the four detector panels; (b) vertical profile across one column of the flood histogram; (c) horizontal profile across one row of the flood histogram.

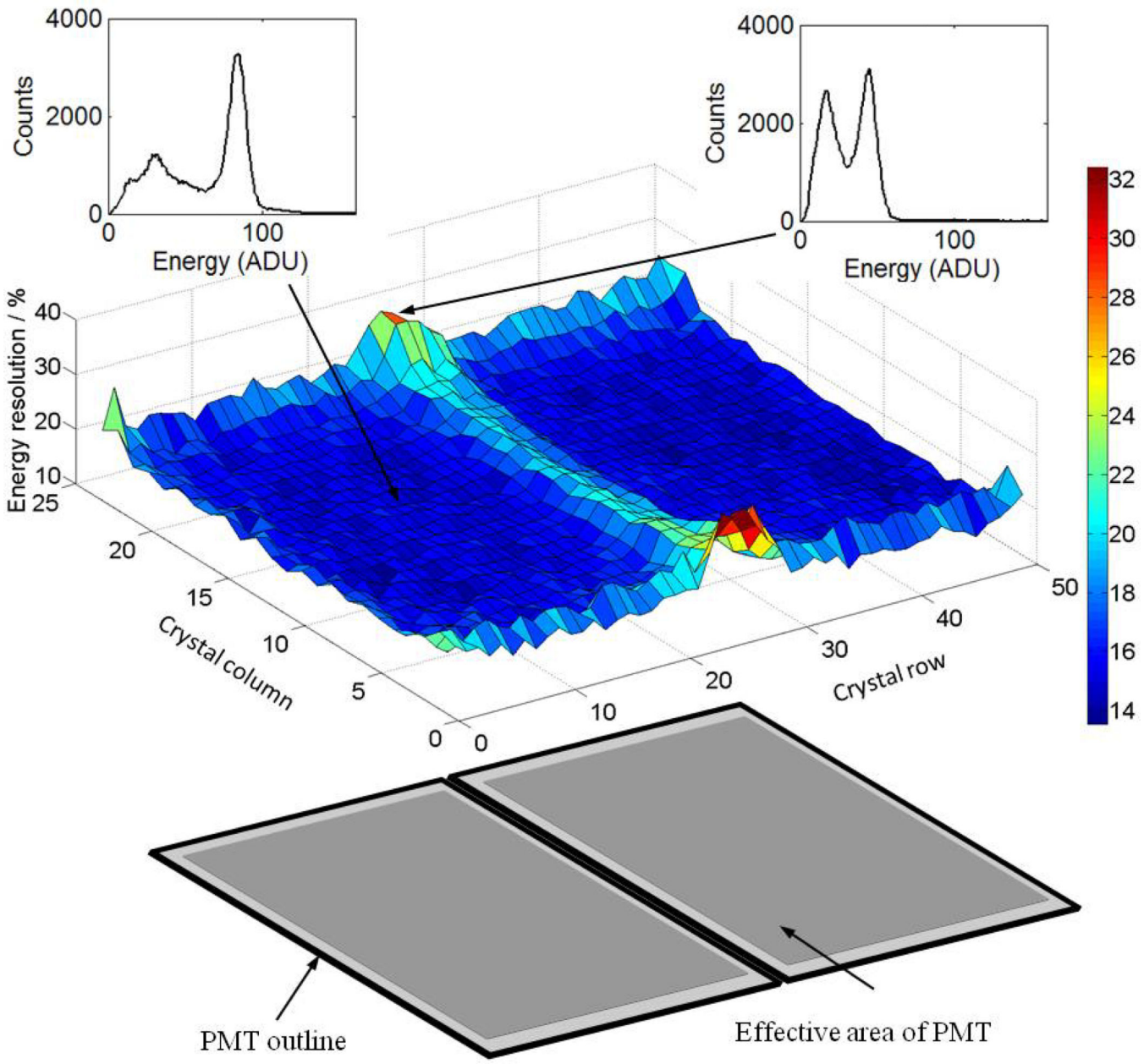

Figure 4.

Position dependent energy resolution for one of the detector panels, superimposed on a map of the active areas of the two PSPMTs that make the detector panel. The measured energy spectra for two representative crystals at the center and at the edge of the detector panel are shown here.

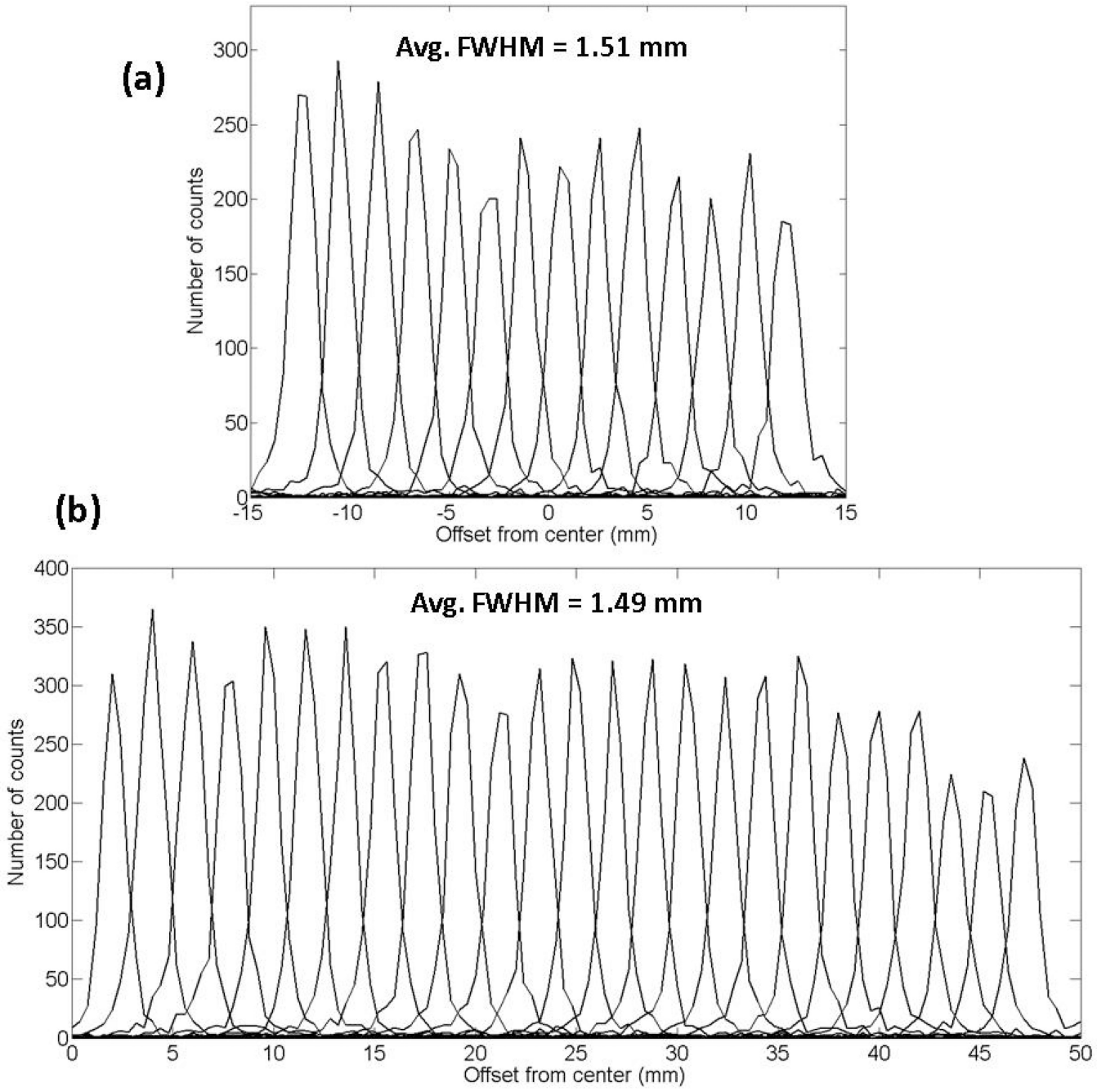

Figure 5.

Intrinsic spatial resolution measured with a ^{22}Na point source in the direction (a) along the detector short axis and (b) along the detector long axis.

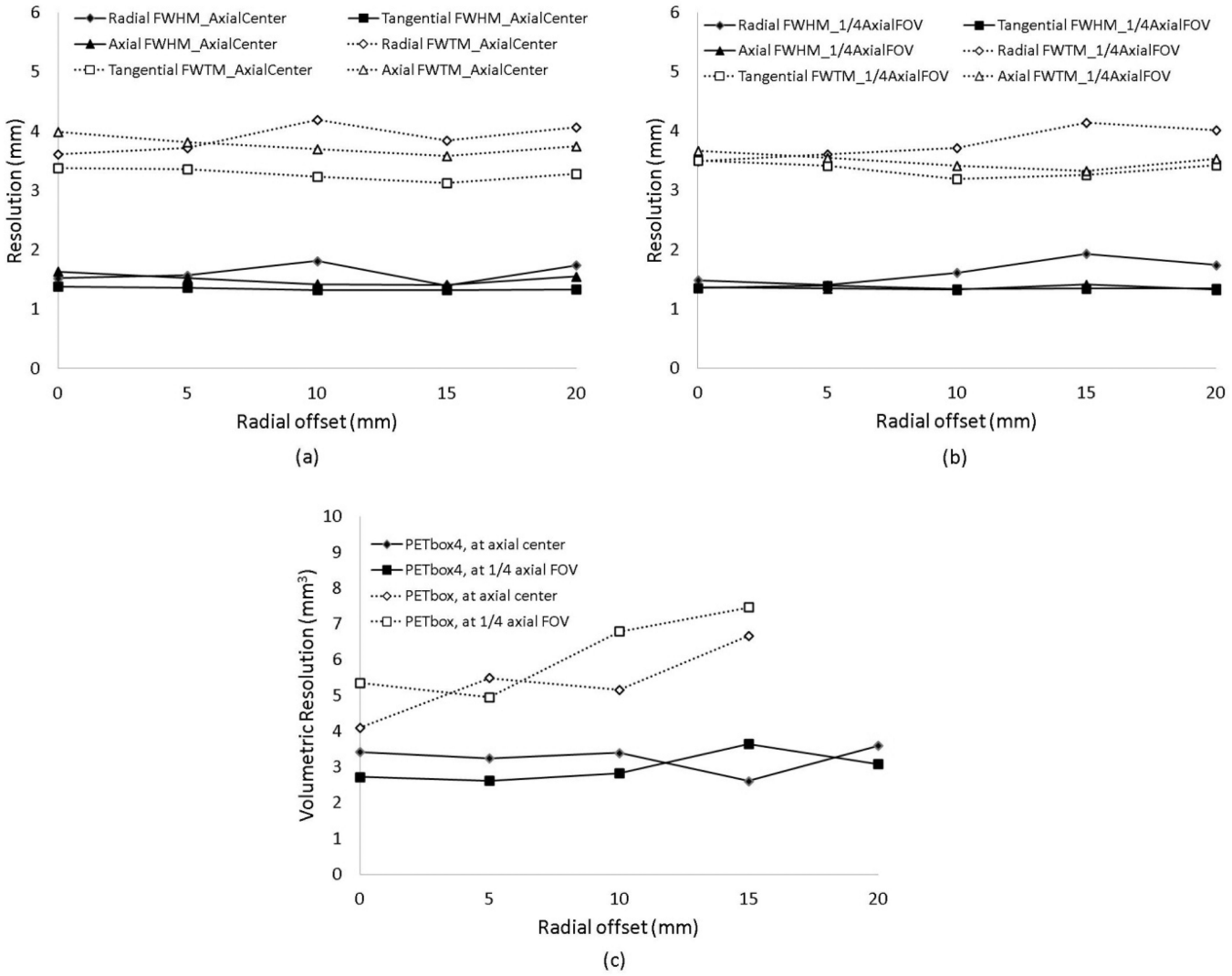

Figure 6.

ML–EM reconstructed image spatial resolution of the PETbox4 system plotted per the modified NEMA NU-4 protocol, showing the FWHM and FWTM of the radial, tangential, and axial image resolutions at (a) axial center of the FOV and (b) 23.5 mm from the axial center towards the axial edge of the FOV. (c) The volumetric resolution of the PETbox4 compared with the PETbox.

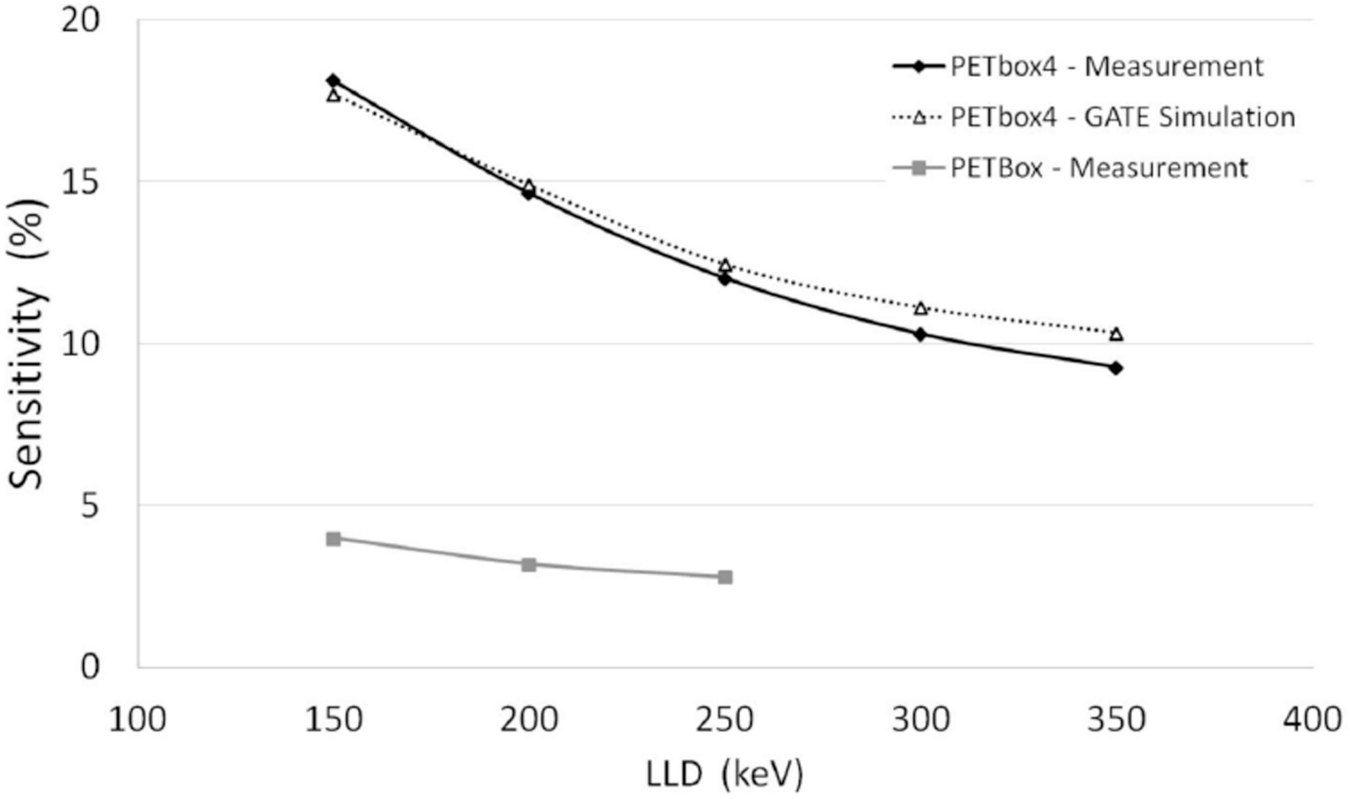

Figure 7.

Absolute peak system sensitivity as a function of lower-level discriminator (LLD) for the PETbox4, the PETbox and the GATE simulation.

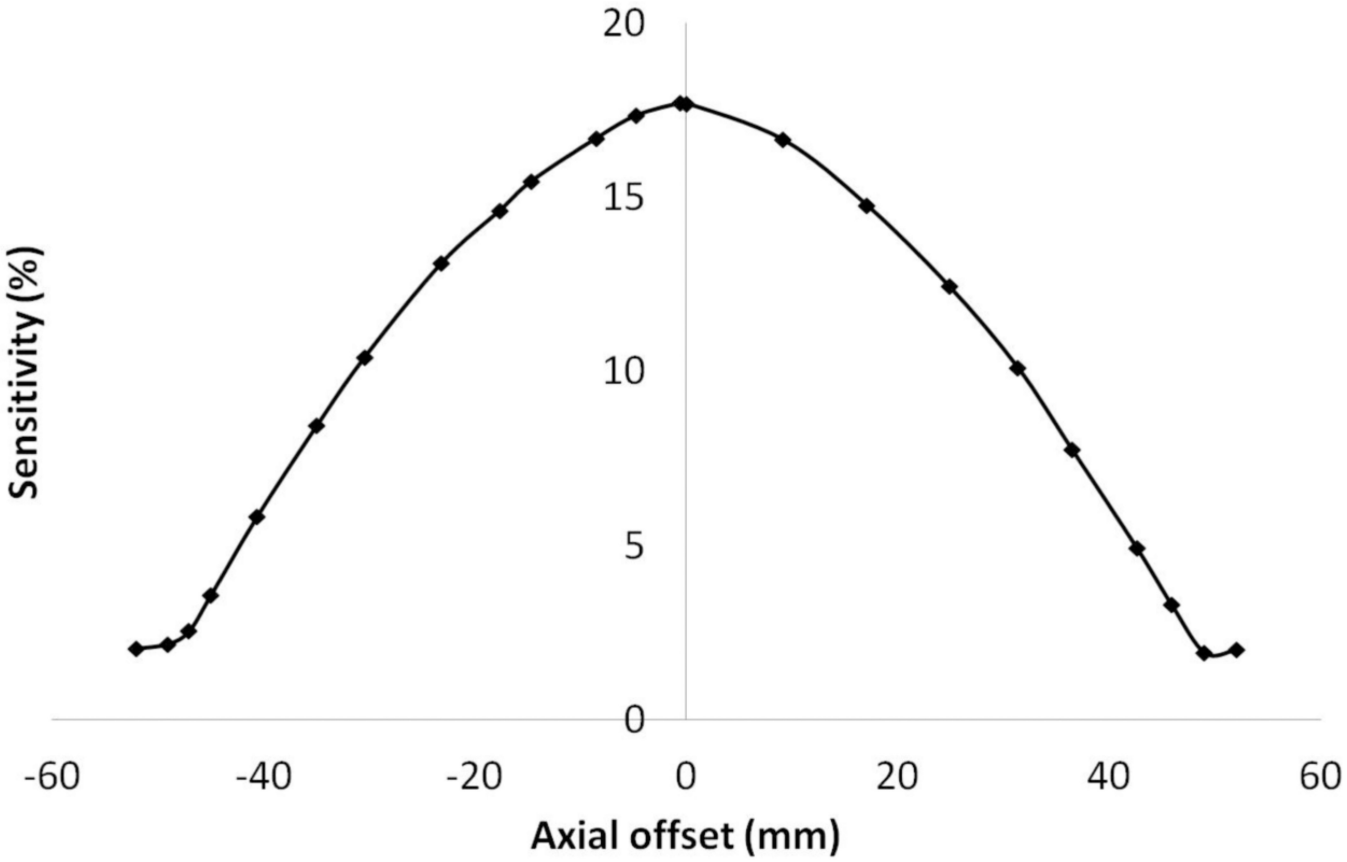

Figure 8.
PETbox4 sensitivity profile as a function of axial position. The energy window was 150–650 keV.

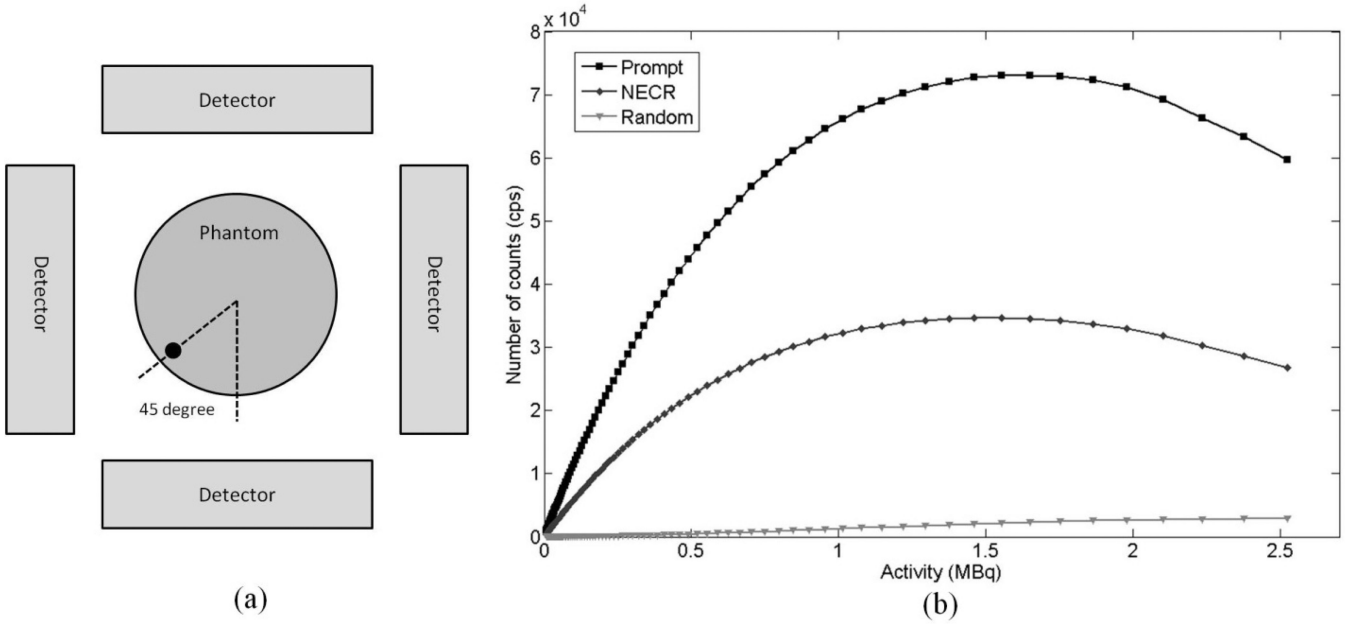

Figure 9.

(a) Schematic drawing of the experimental setup for the count rate performance measurement. The phantom was centered in the FOV and rotated by 45 degrees. (b) Count rate capability of the PETbox4 system as a function of the line source activity. Energy window was set at 150–650 keV.

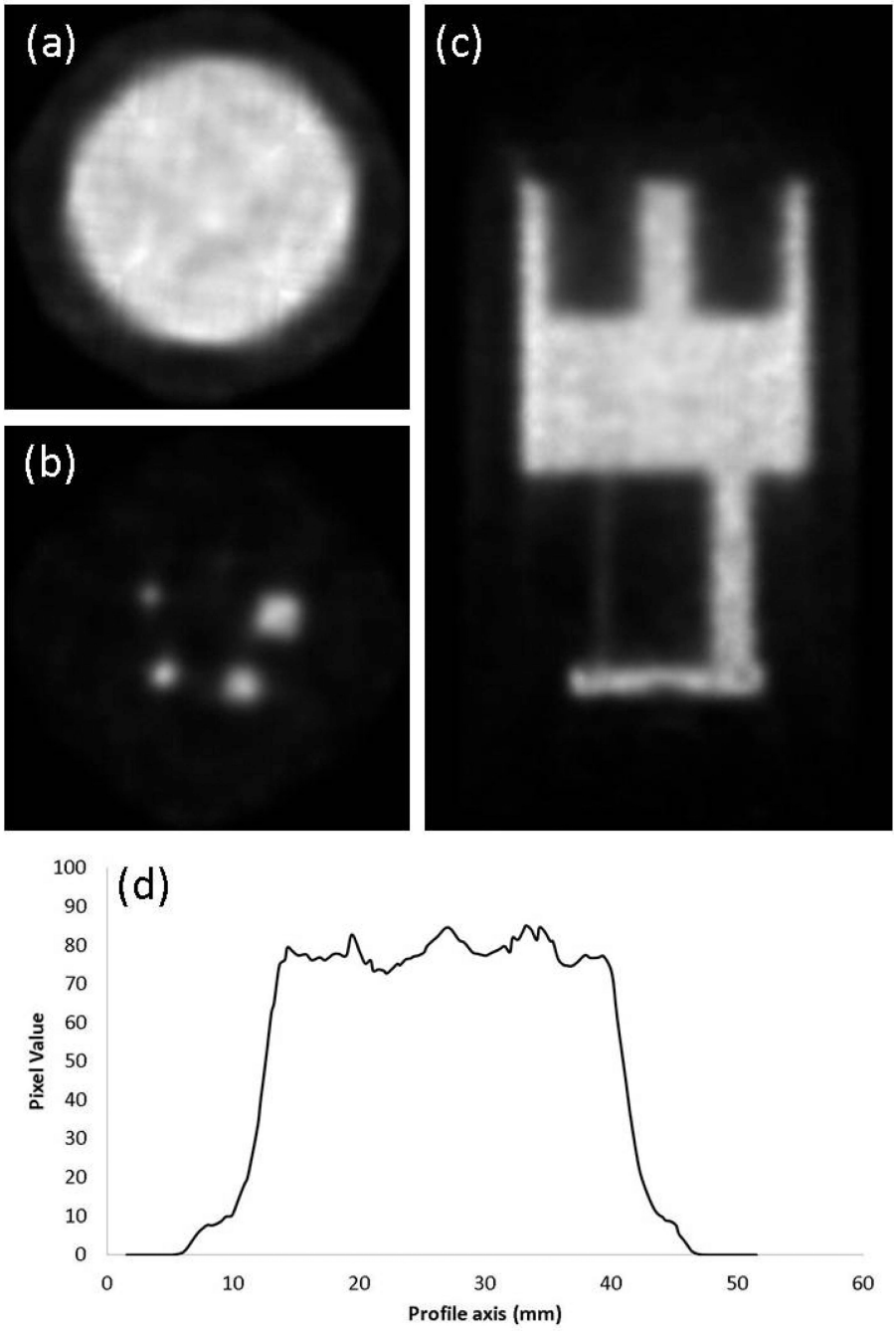

Figure 10.

Image reconstruction of the NEMA NU-4 image quality phantom scanned for 20 min with ^{18}F (1.85 MBq). (a) A transverse slice of the uniform region; (b) A transverse slice of the rods region; (c) A coronal slice; (d) A profile across the uniform area.

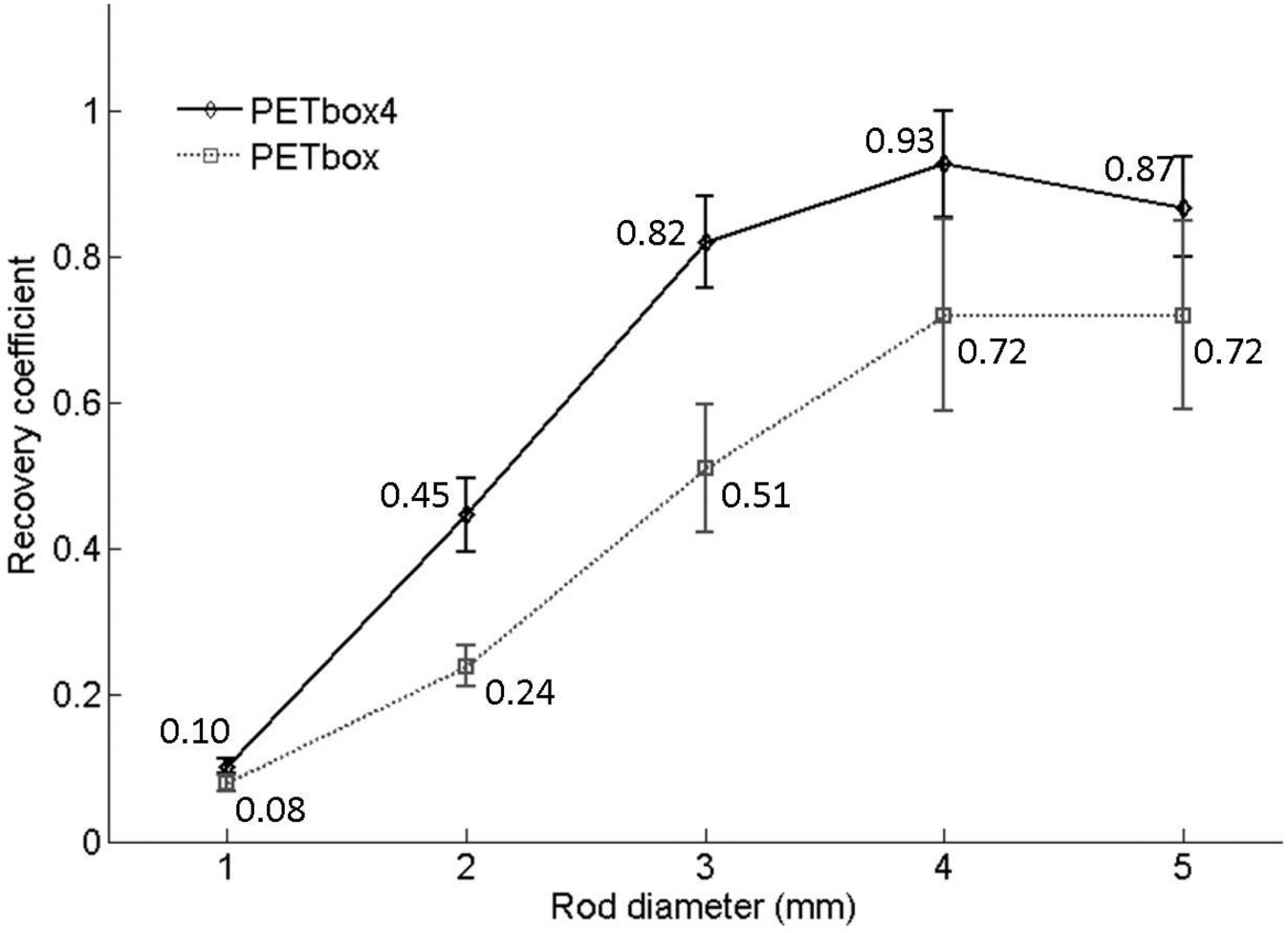

Figure 11.

Recovery coefficients and standard deviations for five rods of different sizes for the PETbox4 and PETbox systems.

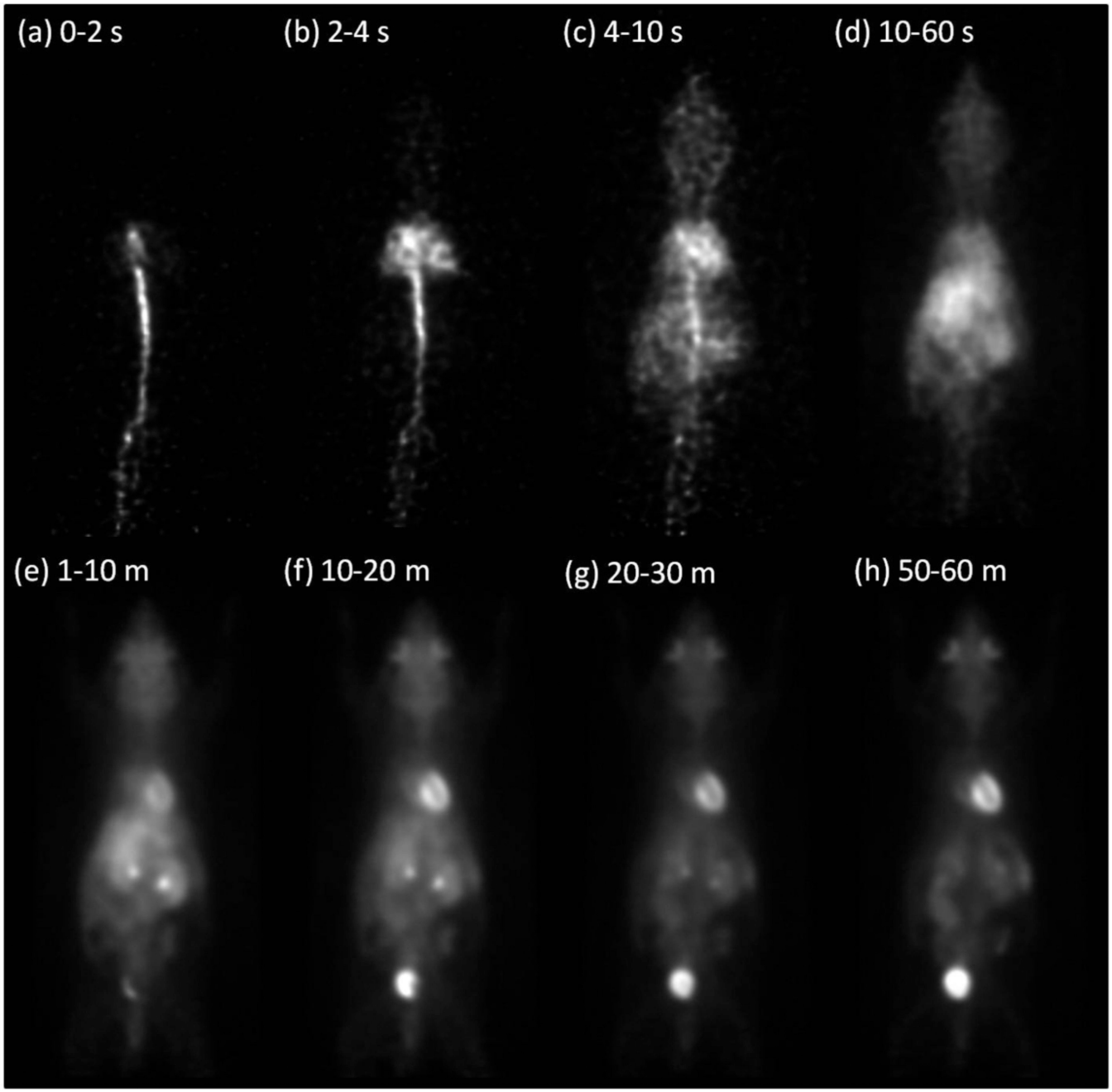

Figure 12.

Selected frames from the 1 hour dynamic scan of a mouse following a tail injection of 1.59 MBq (43 μCi) [^{18}F]-FDG. Different coronal AIP images are shown for each frame to better reveal the activity distribution for different time periods.

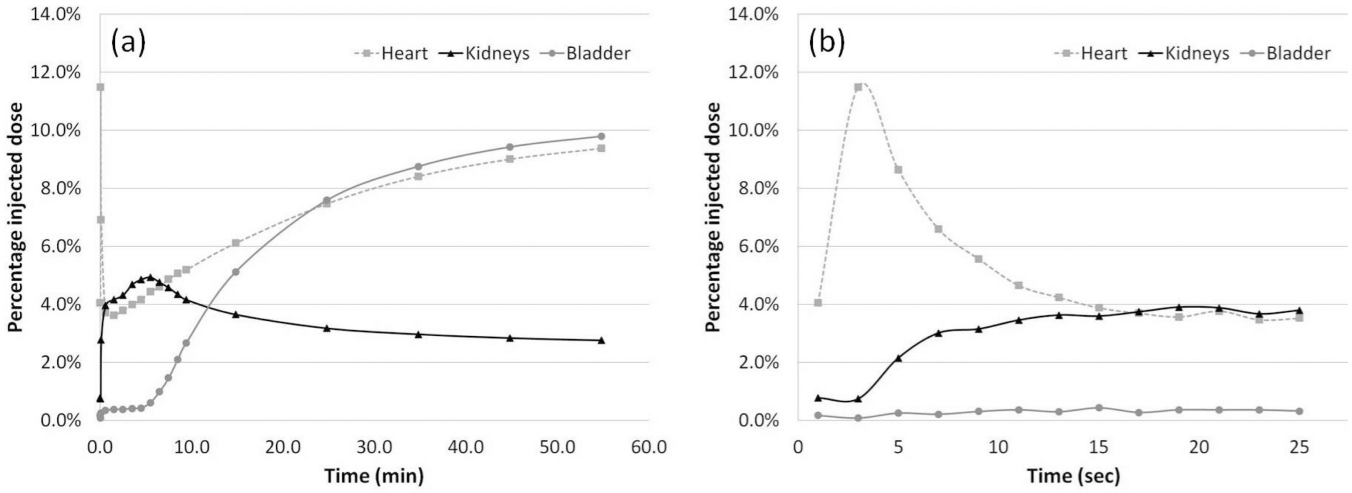

Figure 13.

Time activity curves in major organs of a mouse during the 1 hour dynamic [^{18}F]-FDG scan. (a) Organ uptake for the 1 hour period. (b) A detailed graph showing the first 26 s following injection. Data was reframed to better display the early changes.

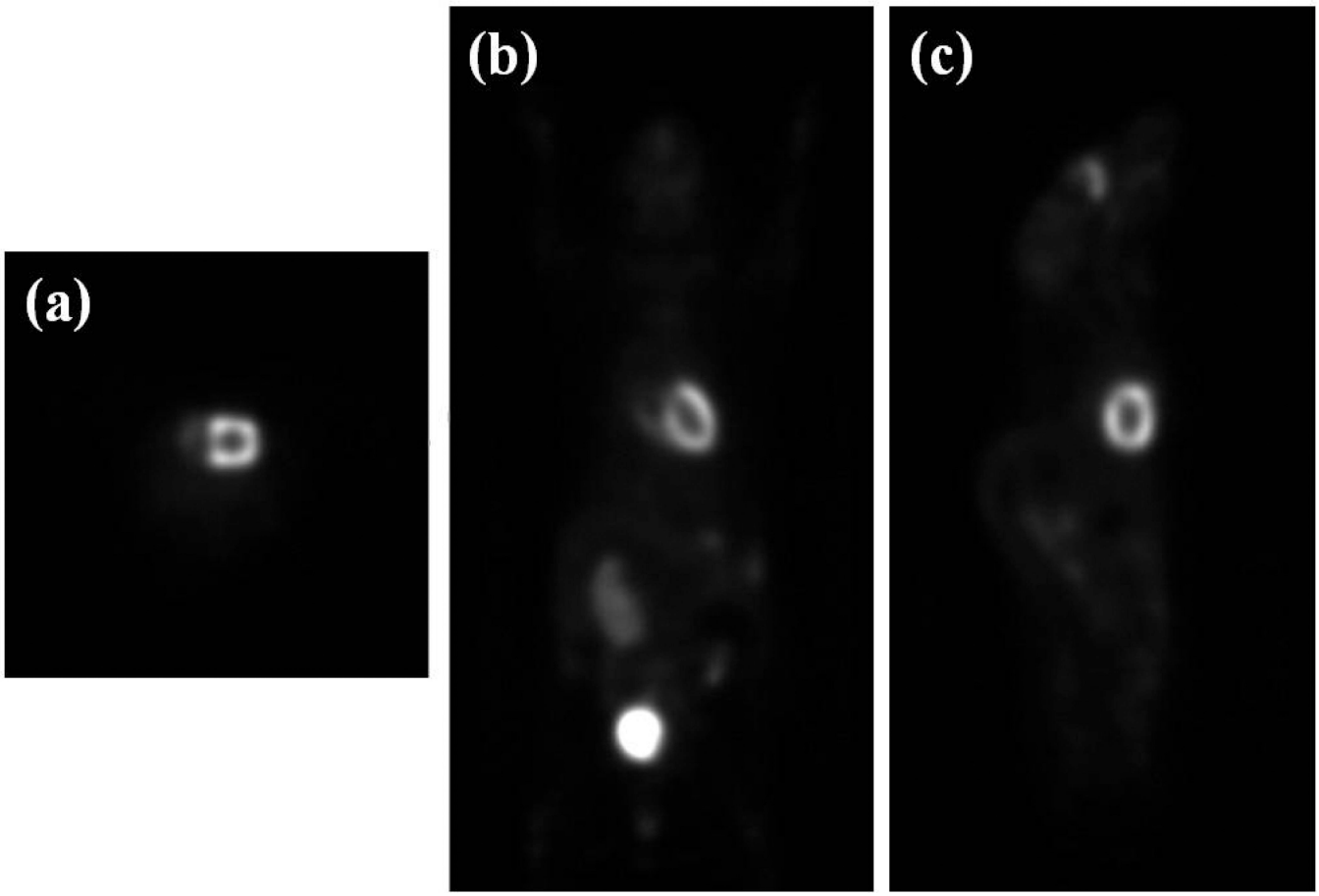

Figure 14.

Reconstructed transverse (a), coronal (b) and sagittal (c) slices showing the uptake of [^{18}F]-FDG in heart and bladder in a healthy mouse during a 10 min scan acquired 50 min after injection. The activity was 0.93 MBq (25 μCi).

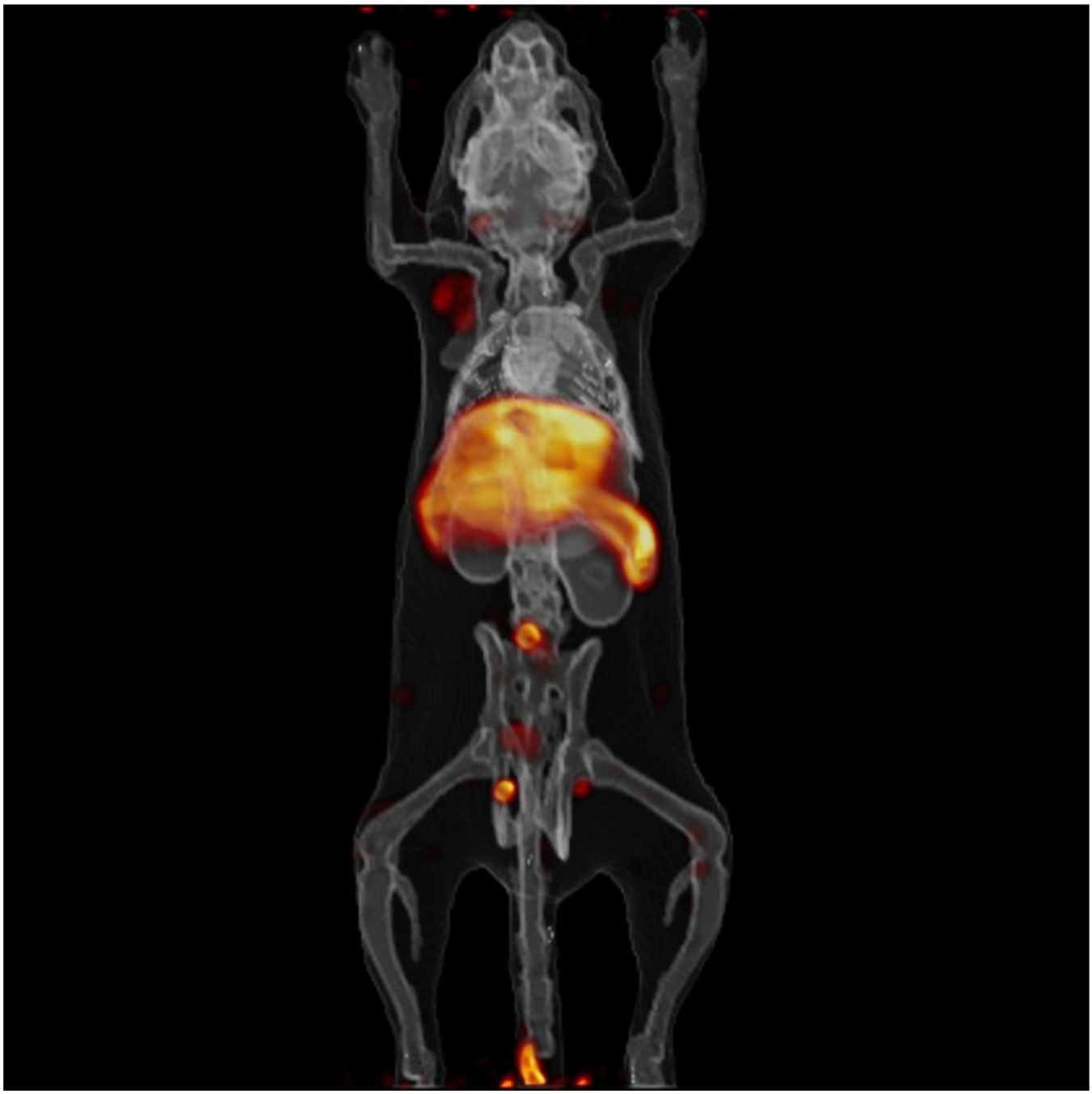

Figure 15.

Selected reconstructed three-dimensional volume rendered image with MARS registration showing the uptake of ^{64}Cu radiolabeled minibody in liver in a healthy mouse during a 20 min scan after an uptake of 4 hours. The activity was 0.14 MBq (3.7 μCi) in the entire mouse at the scan time.

Table 1

Characteristics of the PETbox and the PETbox4 system

		PETbox	**PETbox4**
Detector	Crystal material	BGO	BGO
	Crystal size	2 × 2 × 5 mm^3	1.82× 1.82 × 7 mm^3
	Crystal pitch	2.2 mm	1.90mm
	Packing fraction	0.83	0.92
	Crystal Array	20 × 44 crystals/PMT	24 × 50 crystals/PMT
	PMTs	Hamamatsu H8500 PSPMT	Hamamatsu H8500 PSPMT
	Reflector between crystals	NA	VM2000
System	Number of detectors	2	4
	Number of crystals	1760	4800
	Axial FOV	96.8mm	95mm
	Transaxial FOV	44mm	45mm

Table 2

Energy resolution of the four detector panels in the PETbox4 System

Detector	Mean	Max	Min
0	19.76	42.25	15.54
1	17.48	48.31	13.81
2	16.91	32.39	13.53
3	17.41	35.96	13.89
Overall	17.89	48.31	13.53